FFI-RAPPORT

20/02365

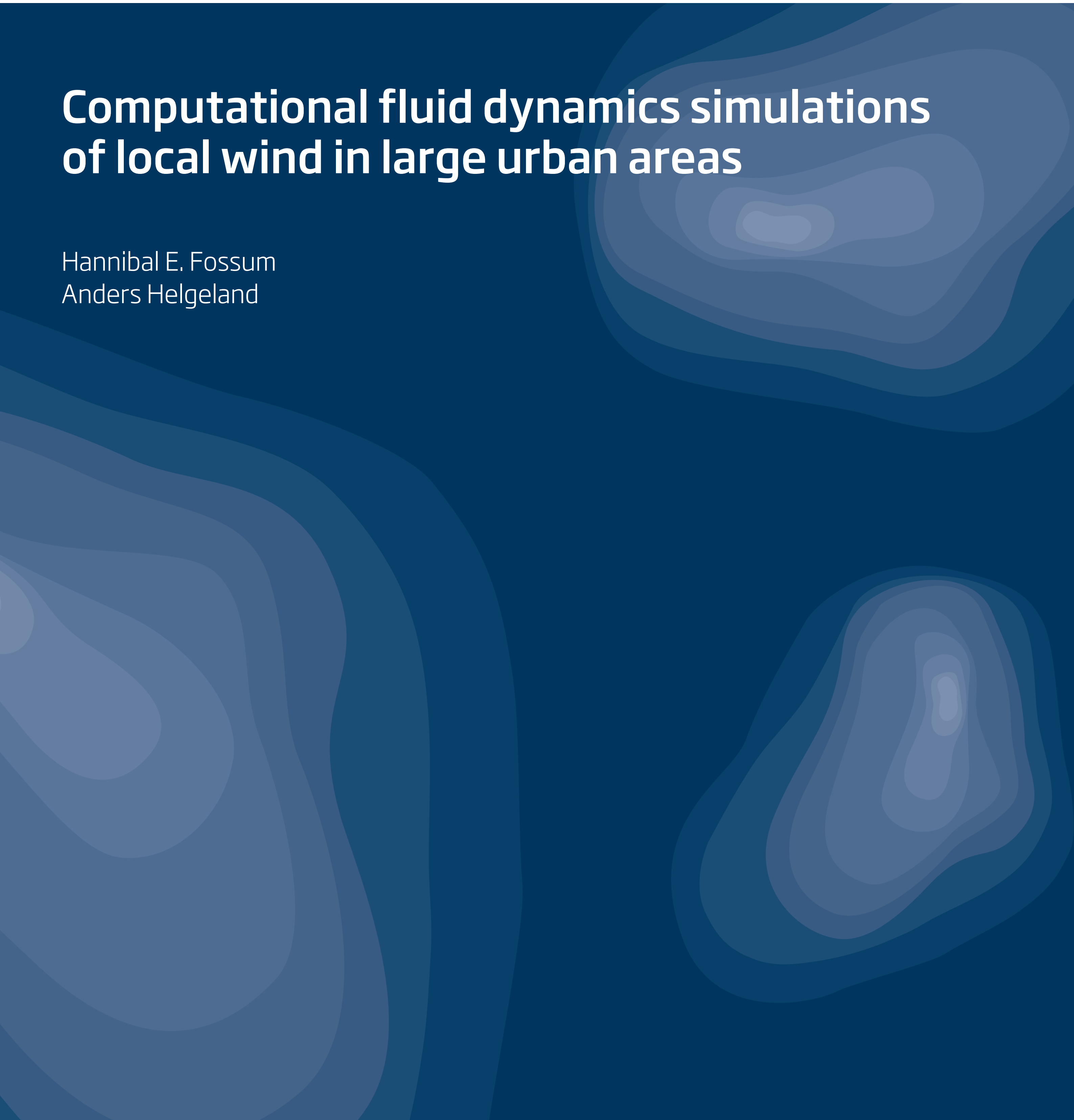

Computational fluid dynamics simulations of local wind in large urban areas

Hannibal E. Fossum
Anders Helgeland

Computational fluid dynamics simulations of local wind in large urban areas

Hannibal E. Fossum
Anders Helgeland

Norwegian Defence Research Establishment (FFI) 29 September 2020

Keywords
Bymiljø
CBRN-vern
Computational Fluid Dynamics (CFD)
Matematisk mekanikk
Spredningsmodellering
Vind

FFI-rapport
20/02365

Project number
1394

ISBN
E: 978-82-464-3289-2

Approvers
Janet M. Blatny, *Research Director*
Anders Helgeland, *Research Manager*

The document is electronically approved and therefore has no handwritten signature.

Copyright

(U) Summary

The present report details the methodology and parameters used for high-fidelity computational fluid dynamics (CFD) simulations of wind in large urban areas. In particular, a 150 km^2 area of Oslo is used as an example, and local flows resulting from 18 different meteorological wind directions have been simulated. To the knowledge of the authors, this is the first documented case of large-eddy simulations of complex urban geometries larger than approximately 25 km^2 with geometry-conforming tetrahedral meshes.

The work is presented in the context of the FFI-project “UNOS”, which concerns the development of a high-quality operational hazmat dispersion tool for use in Norwegian cities. Such a tool is valuable for risk assessment, situational awareness and improved preparedness for emergency events involving urban dispersion of chemical or biological agents. That said, the guidelines and workflow discussed are relevant to many cases in which CFD simulations of a geographical area are of interest. Examples include wind-load computations, wind-comfort simulations, and air-pollution simulations. Choices of sufficient mesh resolutions, wind inflow formulations and other parameters relevant to the present context are discussed.

Reported results mainly exemplify flow data from selected simulated global wind directions, and the examples show how such data can be presented. However, in determining the necessary problem parameters, several relevant results are also found: Although a mesh resolution of 1 m close to solid surfaces is recommended, a 2 to 4 m resolution suffices for the specific context of this work. Further, it is shown that the details of a turbulent inflow is not essential. On the other hand, the domain height and wall boundary-conditions have noticeable impacts on the solution; a domain height of 4 km was sufficient for the present case, and weakly imposed wall-boundary conditions perform somewhat better than strongly imposed conditions for the finite-volume solver used here.

Applying the methodology described here, 18 different simulations of urban wind in Oslo were successfully computed and used in the generation of the operational hazmat dispersion tool, CT-Analyst® Oslo.

(U) Sammendrag

Denne rapporten drøfter metodikk og parametere som benyttes for høyoppløste fluiddynamiske simuleringer av vind i store byområder. Et 150 km^2 område av Oslo er brukt som et spesifikt eksempel, og den lokale vinden i byrommet er simulert for 18 ulike meteorologiske vindretninger. Såvidt forfatterne kjenner til er dette er den første dokumenterte beskrivelsen av såkalte LES-simuleringer (“large-eddy simulations”) for urbane områder større en omtrent 25 km^2 med geometri-konforme tetraheder-mesh.

Arbeidet presenteres i sammenheng med FFI-prosjektet “UNOS”, som dreier seg om utvikling av et presist operasjonelt verktøy for spredningsberegninger i norske byer. Et slikt verktøy har nytteverdi for risikoanalyser, situasjonsforståelse og bedret beredskap med tanke på spredning av kjemiske eller biologiske trusselstoffer i urbane områder. Arbeidsflyten og føringene som diskuteres i rapporten er imidlertid relevante for mange andre tilfeller der fluiddynamiske simuleringer av vind i et gitt geografisk område er av interesse. For eksempel kan vindlaster, vindmiljø i byrom og luftforurensning simuleres. Valg av tilstrekkelig mesh-oppløsning, gode beskrivelser av det innkommende vindfeltet og andre relevante parametere blir drøftet.

Resultatene er hovedsakelig eksempler på vinddata fra simuleringer for utvalgte meteorologiske vindretninger, og eksemplene viser hvordan slike data kan presenteres. Undersøkelsen av ulike problemparametere avdekket dessuten flere relevante resultater: Selv om en mesh-oppløsning på 1 m nær faste vegger anbefales, er 2 til 4 m oppløsning godt nok for dette arbeidet, gitt konteksten beskrevet i forrige avsnitt. I tillegg viser det seg at detaljene i et turbulent innkommende vindfelt ikke er avgjørende for det urbane vindfeltet. På den annen side vil domenehøyde og grensebetingelser på vegger påvirke løsningen; en domenehøyde på 4 km var tilstrekkelig for simuleringene i dette arbeidet, og en svak formulering av grensebetingelsene ga noe bedre resultater enn en sterk formulering med endelig-volum-løseren som er blitt brukt her.

Metodikken og parametrene beskrevet her er brukt til å simulere urban vind i Oslo for 18 ulike meteorologiske vindretninger, og disse resultatene er videre brukt til å kompilere det operasjonelle spredningsberegningsverktøyet, CT-Analyst® Oslo.

Contents

I Background

II Computational simulation

III Results

IV Concluding remarks

Appendix

Abbreviations

The following abbreviations are introduced and used in the text:

ABL	atmospheric boundary layer
CFD	computational fluid dynamics
GIS	geographic information system
IED	improvised explosive device
LES	large-eddy simulation
NRL	Naval Research Laboratory
RANS	Reynolds-averaged Navier-Stokes
RMS	root-mean-square
TKE	turbulence kinetic energy
UTM	Universal Transverse Mercator coordinates

PART I

Background

1 Introduction

1.1 Motivation

In the context of urban safety, air dispersion of hazardous materials (hazmats) comprises a potential threat to public health. Whether the release of a chemical, biological or radiological agent is accidental (e.g., from an industrial incident) or intentional (e.g., from a terrorist attack), the agent is ultimately dispersed by means of turbulent winds for distances which may range up to several kilometers or more.

The application of dispersion models to predict hazmat dispersion in urban areas has a range of uses: It can have a preventative effect as an aid in decision-making (i.e., risk-management) related to city planning, transportation routes, resource allocation, etc. Furthermore, it may play a part in emergency preparations through personnel training or consequence analyses. In the event of an actual emergency, an easily accessible and fast model could be used operationally and yield useful information about contaminated areas, danger zones, evacuation routes, etc. Finally, dispersion models can be employed after the occurrence of a hazmat incident. For example, dispersion models may help determine the location and size of the hazmat source, if unknown (so-called "backtracking").

The National Strategy for CBRNE-preparedness in Norway (Ministry of Justice and Public Security, Ministry of Health and Care Services, Ministry of Defence, 2016) as well as a recent White Paper to Parliament on societal security (Ministry of Justice and Public Security, 2016) state that improved chemical emergency preparedness is a governmental priority. Use of modeling tools to obtain relevant information to increase situational awareness and aid decision-making is an important step to improve emergency preparedness.

1.2 Fast, reliable and easy-to-use dispersion modeling

Several different dispersion models presently exist, ranging from very simple models based on predefined geometries to high-fidelity methods based on flow physics. These types of models differ both in response time and how accurate they can predict the hazmat dispersion. Previous studies have found that for urban areas, only dispersion models that can account for the effect of buildings (such as the high-fidelity physics-based methods) should be used for emergency preparedness and response (COST Action ES1006, 2015). The high-fidelity methods, however, are very computational intensive and cannot easily be used in an operational setting.

FFI Project 1394 ("Utvikling av nestegenerasjons operative spredningsmodelleringsverktøy", "*Development of next-generation operational dispersion modeling tools*", UNOS), is motivated by the desire to combine high-fidelity physical-flow modeling, so-called computational fluid dynamics (CFD), with a fast-response easy-to-use hazmat dispersion modeling tool suitable for use in urban areas. This report discusses the necessary steps taken in which high-quality urban CFD of "city-sized" areas can be computed to achieve this goal.

This is the second report published in FFI Project 1394. The first report (Fossum et al., 2018) discusses the methodology developed at FFI to generate high-quality computational meshes ("CFD grids") from geographical-information system (GIS) data, i.e., turning maps into CFD models. An important step in the GIS-to-mesh workflow is the creation of a topologically sound three-dimensional model of the urban area. Presently, a 14.5 × 11 km^2 model of Oslo is used in Project 1394. The first report also provides a broader project background, a summary of different kinds of dispersion modelling techniques, as well as an overview of FFI's previous work on dispersion modeling.

Finally, the previous report describes the fast-response hazmat dispersion tool, CT-Analyst® (cf. e.g. Boris et al., 2004; Patnaik and Boris, 2007; Boris et al., 2011), developed at the Naval Research Laboratory (NRL), in which the CFD results from FFI's simulations will be used as underlying data. These topics will be discussed only briefly in the present report.

> Consult the previous project report (Fossum et al., 2018) for a broader project background, a summary of different kinds of dispersion modeling techniques, an overview of FFI's previous work on dispersion modeling, and a more thorough description of the fast-response hazmat dispersion tool, CT-Analyst®.

Whereas the previous report covers the generation of the computational mesh suitable for CFD simulation, the present report documents the simulation procedure per se in more detail. In the following, simulation methodology, mathematical framework and parameter choices will be discussed, as will some illustrative results from the simulations. The model and parameter choices discussed are tailored for CFD simulations that produce acceptable results for CT-Analyst®. The simulation methodology outlined here can be used with other parameter choices (e.g., a higher mesh resolution) to produce results more appropriate for other purposes, such as wind load computations, wind intermittency estimates, or urban canopy modelling.

1.3 CT-Analyst®

CT-Analyst (Contaminant Transport Analyst) (cf. e.g. Boris et al., 2004; Patnaik and Boris, 2007; Boris et al., 2011) is an instantaneous hazard-prediction tool developed by the U.S. Naval Research Laboratory (NRL), to aid in time-critical civil-defense decisions in cities. CT-Analyst works by using pre-computed wind fields based on computational fluid dynamics (CFD) simulations with highly detailed urban geometry. The simulation results are post-processed and compressed to be instantly available in the software. CT-Analyst® can thus provide answers in milliseconds with more accurate information than industry-accepted "Puff/Plume" models that take several minutes to run. In addition to fast and accurate hazard predictions, CT-Analyst® enables capabilities such as sensor fusion, backtracking to determine unknown source locations, and computation of building danger zones and sensor coverage areas. NRL have previously developed operational versions of CT-Analyst® for several U.S. cities in addition to Hamburg (Germany).

CT-Analyst® is intended for use in hazmat dispersion events on the 100 m to 10 km scale. Furthermore, the predictions need to be conservative in the sense that the concentration levels reported at a given location should never be less than what could be encountered in a real incident with the same scenario parameters. A prediction error for the edge of the hazmat plume of O(10 m), i.e., from 5 to 50 m, is acceptable in CT-Analyst as long as it is on the conservative side, i.e., widens the plume. These considerations also have implications for the required level of accuracy of the CFD simulations; most importantly, underprediction of the turbulence levels (and hence turbulent mixing) should be avoided – or at least accounted for via global tuning parameters in CT-Analyst.

The present simulation results are primarily intended to be used for dispersion calculations in a new version of the fast-response software tool, CT-Analyst® Oslo, in the following referred to simply as "CT-Analyst".

1.4 Objectives

The American Institute of Aeronautics and Astronautics (AIAA) defines validation as “the process of determining the degree to which a model is an accurate representation of the real world from the perspective of the intended uses of the model” (American Institute of Aeronautics and Astronautics, 1998). When CT-Analyst computes its dispersion predictions, it relies on a database of CFD-computed mean and root-mean-square wind velocities at several vertical elevations above ground. These are thus the primary quantities of interest from the present CFD simulations and need to be sufficiently accurate and reliable for an acceptable end-result in CT-Analyst.

That said, hazmat dispersion will also be computed in the CFD simulations directly, both for comparison with and global tuning of the CT-Analyst predictions, and to study the dispersion in more detail than is possible from CT-Analyst data.

The model and parameter choices discussed in the present report are tailored for simulations that produce acceptable results for CT-Analyst hazmat predictions. As previously mentioned, the simulation methodology outlined here can be used with other parameter choices as well, to produce results more appropriate for other purposes.

The objectives of the CFD simulations described in this report are thus as follows:

- Investigate the ability to perform high-fidelity numerical simulations of fluid flow in large, complex urban environments (entire cities) with software and hardware currently at FFI.
- Determine appropriate model and parameter choices for such simulations.
- Produce simulation results that are well-suited for predictions of hazmat concentration levels in the separate fast-response tool, CT-Analyst.

2 CFD simulations of urban flow

CFD, described in more detail in Part II, concerns the solution of fluid-dynamical conservation equations by means of numerical methods on a computer system. The goal of CFD is thus the ability to predict fluid flow reliably for a given problem or scenario.

Due to increased computational capabilities, CFD has become a standard tool for urban wind and dispersion simulations in recent decades.[1] Though not highly prevalent in the literature, comparisons with wind-tunnel experiments generally indicate that careful execution and analysis of CFD computations give good predictions of real-life fluid-flow behavior in an urban context (Lien and Yee, 2004; Coirier et al., 2005; Hanna et al., 2006; Lien et al., 2006; Santiago et al., 2007; Patnaik et al., 2009; Hertwig et al., 2017a,b; Lateb et al., 2016). At FFI, the CFD framework have been used with both idealized and real urban areas for a range of applications (Wingstedt et al., 2012; Fossum et al., 2012; Gjesdal et al., 2013; Vik et al., 2015; Wingstedt et al., 2017; Fossum and Helgeland, 2019).

So-called Reynolds-averaged Navier-Stokes (RANS) modeling, in which the effects of turbulence on the mean flow are represented by large-scale models, has been the most common approach to urban wind and dispersion simulations, and examples of such simulations are abundant (Blocken et al., 2013; Tominaga and Stathopoulos, 2013; Lateb et al., 2016). RANS models are relatively quick to employ, and their boundary conditions are easier to prescribe than for more complex modeling approaches. However, a lack of spatial and temporal details as well as a lack of generality, resulting in a range of different submodels and parameter choices, are well-known disadvantages. RANS models also commonly suffer from inadequate representation of flow-history effects, low-turbulence regions and turbulence anisotropy (Durbin and Petterson Reif, 2011).

In more recent years, large-eddy simulation (LES) of urban wind and dispersion has also become widespread (Pullen et al., 2005; Gousseau et al., 2011; Blocken et al., 2013; Tominaga and Stathopoulos, 2013; Lateb et al., 2016; Tominaga and Stathopoulos, 2016; Dai et al., 2018; García-Sánchez et al., 2018; Tolias et al., 2018). In the LES modeling approach, only the smaller scales of turbulence are modeled, whereas all larger scales of motion are resolved numerically. Urban LES simulations result in full three-dimensional and temporal data sets, which must be sampled over time to calculate turbulence statistics. There is less need for model tuning than in RANS models, and turbulent motion is generally reproduced more accurately and in more detail. In an urban context, LES appears to be particularly well-suited, owing – among others – to the significant role of geometry effects, wind anisotropy and large temporal concentration-value excursions (Tominaga and Stathopoulos, 2013; Lateb et al., 2016; García-Sánchez et al., 2018).

More general introductions to RANS and LES modeling can be found in e.g., Pope (2000) and Sagaut (2006), respectively. More thorough information on FFI's LES methodology, including details pertaining to the conservation and subgrid-model equations, can be found in Fossum et al. (2018).

To date, most CFD simulations in urban areas – even with the relatively cheap RANS approach – have been performed on rather small computational domains, typically between 0.1 and 4 km^2, such as those reported in previously listed references. Notable exceptions are the simulations of Pullen et al. (2005); Patnaik et al. (2009); Hertwig et al. (2017a), all computed within the same

---

[1] In the present context, the concept of "urban CFD" concerns only CFD simulations in which the buildings are resolved to at least some degree. Mesoscale CFD modeling, in which urban areas are represented as roughness or porous regions, is a different matter that will not be discussed here. Interested readers can consult e.g., Fernando (2012) for a broader overview of urban CFD.

research group at the NRL by using rather coarse Cartesian cut-cell meshes. Another remarkable example of a large-domain urban CFD is the astonishingly large simulation of a 25×25 km^2 area of Tokyo by Tamura et al. (2015), numbering a staggering 25 billion computational mesh cells, also on a cut-cell mesh. However, apart from the very brief conference contribution cited above, little documentation of the latter simulation is found.

To the knowledge of the authors, no urban LES (or even RANS) simulation has been performed in which a tetrahedral geometry-conforming mesh has been used in conjunction with large ($\gtrsim$ 25 km^2) domains. This report thus appears to be the first documentation of such simulations. The benefits of (tetrahedral) geometry-conforming meshes will be discussed in Section 5.2.

3 Structure of the report

The aim of this first part of the report is to provide the necessary background and context for the methodology and results presented in the remainder of the report. A broader project introduction than what is given here can be found in Fossum et al. (2018), if needed.

In Part II, the methodology of the wind and dispersion simulations is discussed. The first chapter briefly shows the mathematical equations governing the fluid flow and dispersion, thus providing a mathematical framework for the CFD methodology. The second chapter will summarize the more practical aspects of CFD, including the general workflow. Finally, the last chapter of Part II discuss the specifics of the present simulations. Here, results pertaining to effects of model parameters are included.

Part III aims to convey a selection of relevant results from the wind and dispersion simulations, exemplifying how such data can be interrogated and presented.

Finally, concluding remarks and plans for future work are presented in Part IV.

PART II

Computational simulation

4 Mathematical background

4.1 Governing equations

The governing equations of fluid motion state that mass and momentum are conserved, and they are thus referred to as conservation equations. The conservation equation for momentum follows from Newton's second law.

In the following, index notation is used in conjunction with Einstein's summation convention. Unless stated otherwise, free indices range from 1 to 3, and repeated indices imply summation.

A Cartesian coordinate system is assumed. The general spatial position vector is given by

$$\boldsymbol{x} = (x_1, x_2, x_3) = (x, y, z),$$

whereas time is denoted t. x and y are horizontal coordinates in eastward and nortward directions, respectively, whereas z is taken as the vertical direction. The corresponding three-dimensional instantaneous-velocity vector field is denoted

$$\begin{aligned}\tilde{\boldsymbol{u}}(\boldsymbol{x}, t) &= (\tilde{u}_1(\boldsymbol{x}, t), \tilde{u}_2(\boldsymbol{x}, t), \tilde{u}_3(\boldsymbol{x}, t)) \\ &= (\tilde{u}(\boldsymbol{x}, t), \tilde{v}(\boldsymbol{x}, t), \tilde{w}(\boldsymbol{x}, t)),\end{aligned}$$

and the three-dimensional instantaneous-pressure field is denoted $\tilde{p}(\boldsymbol{x}, t)$. Moreover, partial differentiation is abbreviated by

$$\begin{aligned}\partial_i &= \partial/\partial x_i = (\partial/\partial x, \partial/\partial y, \partial/\partial z), \\ \partial_t &= \partial/\partial t,\end{aligned}$$

for spatial and temporal gradients, respectively, when this is beneficial.

The conservation equations for momentum and mass for an incompressible, Newtonian fluid can thus be written

$$\partial_t \tilde{u}_i + \tilde{u}_k \partial_k \tilde{u}_i = -\frac{1}{\rho}\partial_i \tilde{p} + \nu \partial_k \partial_k \tilde{u}_i + F_{V,i}, \tag{4.1}$$

$$\partial_k \tilde{u}_k = 0, \tag{4.2}$$

respectively. Here, ρ is the (constant) fluid density and $\nu = \mu/\rho$ is the kinematic viscosity, with μ being the dynamic viscosity. The term $F_{V,i}$ represents any other volume forces affecting the fluid, such as buoyancy (gravitation) or rotation.

If scalars, such as gases or temperature, are transported passively in the fluid, each of them is also governed by its own transport equation, reading

$$\partial_t \tilde{c} + u_k \partial_k \tilde{c} = \gamma \partial_k \partial_k \tilde{c}, \tag{4.3}$$

in which $\tilde{c} = \tilde{c}(\boldsymbol{x}, t)$ is the transported scalar, and γ is its diffusivity.

For the system of partial differential equations to have a unique solution, initial and boundary conditions must also be provided.

The second term on the left-hand side of Eq. (4.1) is the advective term. Its nonlinearity makes the solution of this equation system highly susceptible to minimal perturbations in initial and boundary conditions, which in turn may lead to a turbulent solution. The nonlinearity generally renders the equations impossible to solve analytically. For most flow systems, approximate models related to this nonlinearity are utilized, so-called *turbulence models*.

In the simulations described in the following, the flow turbulence arising from the nonlinear nature of Eq. (4.1) is modeled through so-called large-eddy simulation (LES), based on decomposition of fluid flow fields into *resolved* and *subgrid* (unresolved) parts, e.g., $\tilde{u}_i^r(\boldsymbol{x}, t)$ and $\tilde{u}_i^s(\boldsymbol{x}, t)$, respectively, for the velocity field. This decomposition and filtering procedure introduces an additional model term, so-called subgrid stresses, on the left-hand side of Equation (4.1) (and similarly for transported scalars), but otherwise the equation remains similar in form.

Despite the advantages of LES in predicting details of turbulent flows, near-wall treatment at high Reynolds numbers remains a challenge. At lower Reynolds numbers, the viscous, high-shear region close to solid boundaries may be fully resolved, but for most real-life flows, this is unfeasible. If wall-generated shear is the main instigator of turbulence, near-wall modeling akin to Reynolds-averaged Navier-Stokes (RANS) wall models must be employed to obtain reasonable results. However, if other turbulence sources dominate, e.g., jets, vortex shedding, or shear from geometric roughness, LES may be well-suited. Perhaps unsurprisingly, the latter is the case for urban geometries.

A final concern regarding LES is that of appropriate boundary conditions, particularly in the case of velocity inlets or free-stream boundaries. The prescription of physically realistic conditions consistent with the mathematical models and numerical implementation of a solver is still an area of research, cf. e.g., Keating et al. (2004); Wu (2017). That said, exact boundary conditions are not essential to all studies of turbulent flow.

More information on the mathematical framework discussed above, as well as more details on the filtered equations and subgrid terms pertaining to the LES model used in the present study, can be found in Fossum et al. (2018).

4.2 Flow statistics

A turbulent flow field is random and stochastic in nature (Wyngaard, 2010, p. 15). So-called Reynolds decomposition separates a turbulent field into two parts: By averaging the field, the *mean flow field* is obtained, and the difference between the full field and the mean field then comprises the *fluctuating flow field*. Mathematically, the Reynolds decompositions can be written

$$\begin{aligned} \tilde{u}_i &= U_i + u_i, \\ \tilde{p} &= P + p, \\ \tilde{c} &= C + c \end{aligned}$$

for the velocity field, pressure field and an arbitrary scalar field, respectively. Here, symbols marked by a tilde ($\tilde{\cdot}$) denote full four-dimensional fields – or, in the present case of LES fields, resolved (filtered) four-dimensional fields – whereas the uppercase and lowercase symbols denote mean and fluctuating fields, respectively. Formally, the averaging procedure is an ensemble average of infinitely many flow realizations. In practice, however, a finite spatial or temporal average (or a combination of both) is commonly used when possible. In the following, any average is denoted by angle brackets, i.e., $U_i = \langle \tilde{u}_i \rangle$, which implies temporal averaging (as an approximation to the ensemble average) in the present context, unless stated otherwise.

By utilizing Reynolds decompositions in Eqs. (4.1) and (4.2) and then applying an averaging procedure, the RANS equations are obtained. These equations, not shown here, describe the evolution of the mean flow fields and also form the basis for the RANS class of turbulence models. The transport equation for a mean scalar field, such as the concentration of a gas, can be derived in a similar manner.

The RANS equations are very similar to Eqs. (4.1) and (4.2), with the exception of an additional source term, $\partial_j r_{ij}$, in which r_{ij} is referred to as the Reynolds stresses.[2] This term originates from the advection term in Eq. (4.1). The Reynolds-stress tensor can be written

$$r_{ij} = \langle u_i u_j \rangle,$$

i.e., each tensor component is a single-point correlation between fluctuating velocity vector components. The Reynolds stress tensor does not really represent physical stresses, but it has the same units. Physically, it is associated with momentum transport due to turbulent fluctuations, so-called turbulent momentum flux. Note also that the three normal components of the Reynolds stress tensor correspond to the statistical variances of the three flow velocity components, respectively, thus providing measures of the velocity fluctuations in the flow.

The *turbulence kinetic energy*, often used to estimate the flow turbulence level, is defined by an index contraction on the Reynolds stresses, i.e., $k = \frac{1}{2}\langle u_i u_i \rangle$.

Additional details on turbulence statistics can be found in Fossum et al. (2018), as well as in most textbooks on turbulence (cf. e.g., Pope, 2000; Durbin and Petterson Reif, 2011).

---

[2] In the case of LES, the RANS equations for the resolved fields contain additional subgrid terms as well. Many of these terms are, however, often negligible.

5 Computational fluid dynamics

5.1 General workflow

As discussed in Section 4.1, the governing equations of fluid motion cannot in general be solved analytically. The solution of Eqs. (4.1)-(4.2), as well as possible additional equations, by means of numerical algorithms on a computer is commonly called *computational fluid dynamics* (CFD). The methodology of CFD varies greatly from application to application and software to software, but the general workflow is often as outlined in Figure 5.1. The main steps in the workflow are described in more depth in Fossum et al. (2018). A summary from that report is given in the following.

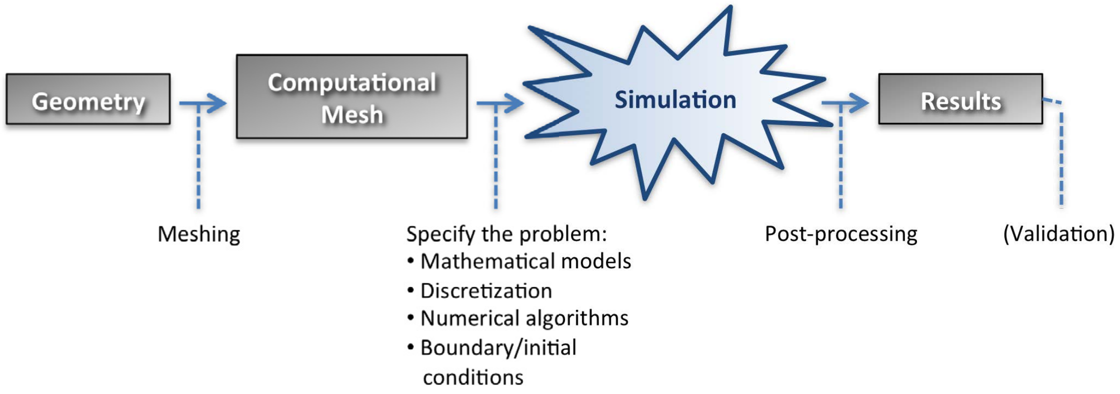

Figure 5.1 Typical CFD workflow (from left to right).

Firstly, the geometry of the problem needs to be supplied, whether this is a simple box or a complex urban area with lots of details. Presently, the geometry – already described thoroughly in Fossum and Helgeland (2017) – is tailored for CFD simulations and can be meshed without further adjustments.

With rare exceptions, the geometry and the volume it encloses must be subdivided into computational *cells* for the CFD solver to give reasonable results. This is a process referred to as *meshing* or *gridding*. The process for meshing urban areas is described in more detail in Fossum and Helgeland (2017).

The equations that are solved in a CFD program come in numerous variants (cf. e.g. Gresho, 1991). Presently, filtered variants of Eqs. (4.1)-(4.2) are implemented.

The equation set needs to be approximated and discretized so it can be solved numerically. For finite-volume method (FVM) solvers, this entails recasting the governing equations in conservative form so that each computational cell in the mesh can be treated as a discrete control volume. The resulting integral system can be discretized, i.e., converted into a system of algebraic equations, by employing a number of substitutions, which depend on the specific variety of FVM used, for the terms in the integrated equations.

For incompressible flows, the discretized equations are then solved for each computational cell in the mesh simultaneously, time step by time step.

The quality of a numerical solver is often judged in terms of its convergence, consistence, and stability (Versteeg and Malalasekera, 1995, p. 6), but in practice versatility and ease-of-use might be equally important. In the context of LES, the numerical algorithm is particularly relevant since the mesh can be relatively coarse.

Conservation of energy is also of particular importance to LES solvers (Mahesh et al., 2004). Hence, the use of robust, non-dissipative numerical algorithms can be crucial to the success of an LES solver.

5.1.1 CDP – a multipurpose LES code

The numerical results discussed in the present report are based on numerical simulations performed with the FVM-based solver CDP v4.0.8 (Mahesh et al., 2002; Ham and Iaccarino, 2004; Mahesh et al., 2004; Ham et al., 2006).

The incompressible version of CDP, `Vida` (previously `Cliff`), stores all flow fields in the mesh nodes. The code is second-order in space and up to second-order in time, using a Crank-Nicholson/Adams-Bashforth time-stepping algorithm. The pressure-coupling is based on a fractional-step approach.

The conceptual calculation of the subgrid viscosity in CDP's dynamic Smagorinsky model is described in Fossum et al. (2018). CDP uses a test filter with twice the size of the ordinary filter width.

The advantages of CDP are similar to those of other FVM-based methods; in particular, the code uses unstructured meshes to be able to handle complex geometries, and it is relatively easy to extend the code by programming additional boundary conditions, source terms or data-processing algorithms. Additionally, the numerical algorithms in CDP are formulated so as to maximize conservation of kinetic energy without loss of numerical stability. Recent versions of the code is written in C++ and is highly parallelized.

The major drawback of FVM-based solvers is reduced accuracy compared to e.g., finite element methods, given similar mesh resolutions.

5.2 Considerations of urban CFD

Any CFD simulation must strike a balance between the optimal quality of the solution and the available computational resources.

In general, a finer computational mesh or a larger compuational domain increase both the quality of the solution and the computational demands. Very roughly, the increase in required computational time scales with $O(3)$ times the increase in mesh points, whereas a given relative extension of the computational domain corresponds to a similar relative extension in required computational time.

Recent studies indicate that urban wind and dispersion simulations should aim towards a 1 m resolution in the area of interest, as well as ensure that larger buildings comprises at least ten computational points in each direction (Xie and Castro, 2009; Franke et al., 2011; Tolias et al., 2018). Other recommendations are also given in the literature, concerning issues such as domain dimensions relative to building and topography features, numerical order-of-accuracies and convergence time periods for statistics (cf. e.g. Franke et al., 2011; Blocken, 2015; Tominaga and Stathopoulos, 2016).

The urban area considered here measures 14.5×11 km^2, implying a significant range of scales in the geometry. Additionally, the Reynolds number of the atmospheric boundary layer (ABL) is large – typically, $\mathrm{Re} \gtrsim 10^6$ – indicating a significant range of scales of the flow. As a result, rather hard compromises are necessary, both in terms of geometric detail and mesh resolution, to be able to run the CFD simulations within a reasonable time frame.[3] As a result, not all of the recommendations in the literature can be followed. Given the intended use of the results, this is deemed acceptable.

As previously mentioned, few urban CFD simulations on large domains use tetrahedral meshes. Instead various Cartesian cut-cell approaches are used, typically with immersed-boundary methods to account for subgrid geometry. Such methods are usually faster and much more robust than geometry-conforming tetrahedral meshing algorithms. The disadvantages, however, are potential stair-casing effects for boundaries that are not aligned with the mesh directions, introducing spurious perturbations into the flow, and rapid changes in cell sizes between different regions, which may reduce numerical accuracy. A geometry-conforming tetrahedral mesh approach is used in this study, as described in Fossum and Helgeland (2017), with high-quality mesh elements, gradual rates-of-change in cell sizes and automatic mesh refinement in narrow streets.

In terms of required averaging-time period, the most relevant time scale in urban flows is the shedding period, i.e., the time period associated with vortex shedding behind a structure. For a simple building, the shedding period depends on the shape and size of the building as well as the wind speed. Typically, the period is in the range of 5 to 90 s, based on geometry dimensions and typical Strouhal numbers. Hence, to capture 10 of the slowest-shedding vortices, a minimum averaging time of 15 minutes (900 s) is needed. For larger hills and cliffs, the shedding periods can be significantly larger than 90 s, so averaging periods of at least one hour is recommended in the present geometry.

By similar arguments, the physics of urban flow implies a maximal numerical time step of around 0.5 s, so that the shortest vortex shedding periods are resolved with at least 10 steps.

For data input to CT-Analyst, 18 different meteorological wind directions need to be simulated. In the following, the wind direction is defined by the clockwise angle from northerly wind, i.e., 0° wind is from the north, 90° wind is from the east and so forth. In order to span the entire wind rose, this means that wind at 20° intervals are simulated. Only one free-stream wind speed needs to be simulated, since the results are independent of the free-stream speed at such high Reynolds numbers (Cui et al., 2017).[4]

5.2.1 Urban flow features

In built environments, such as urban areas, the local wind conditions frequently differ from the (meso-)meteorological wind direction due to local geometric features. The combination of several buildings, and perhaps also topography, yields a complex flow field that is difficult to predict without CFD simulations. That said, basic urban-flow phenomena exist, acting as building blocks for the total wind field developing within the environment as a whole. Examples of such urban-flow phenomena are listed in the following, and some are also illustrated in Figure 5.2.

- **Downdraft (label 1 in Figure 5.2)**: For buildings above a certain height, wind commonly descends on the lower part of the upwind (windward) walls. This downdraft may also instigate helical flow near the ground.
- **Recirculation zones and counterflow (label 2 in Figure 5.2)**: Close to the ground, recirculation zones may form on the leeward side of buildings, where the wind circulates for long periods of time. If several buildings follow in succession, the phenomenon may become more

---

[3] In terms of CT-Analyst employment of the CFD results, there is the additional requirement of running 18 different meteorological wind directions, placing even higher demands on the computational efficiency of the simulations.

[4] The contaminant plume arrival time are an exception, as this scales (globally) with the wind speed.

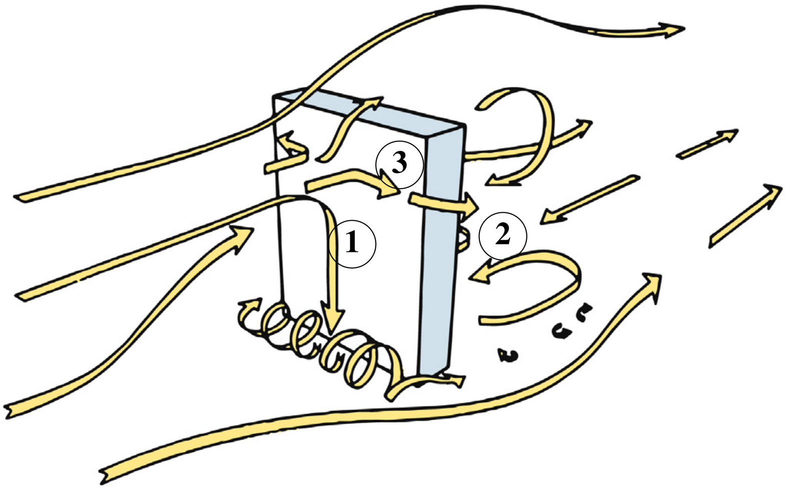

Figure 5.2 Schematic illustration of wind around a single building. Label 1–3 refer to downdraft, recirculation and cross-wind zones, respectively. Adapted from Beranek and Van Koten (1979).

pronounced. Local counterflow wind may also develop associated with the recirculation zones. Recirculation can lead to accumulation of gases or aerosols in such areas over time.

- **Crossflow wind (label 3 in Figure 5.2)**: On the upwind side of buildings, as well as in streets perpendicular to the meteorological wind, significant crosswind may be present.
- **Street channeling**: Long streets often channel the wind very efficiently and thus forces the wind to follow the directions of the streets. As a result, streets may yield crossflow or counterflow wind.
- **The Venturi effect**: Between buildings, and in street canyons, the air flow undergoes contraction. Mass conservation thus implies that the wind velocity increases correspondingly in such areas.
- **Vortex shedding**: Along the edges of buildings (or over curved surfaces), vortices may shed at regular intervals. Such vortices are a significant source of downstream turbulence.

6 Problem-specific considerations

6.1 Problem description

In the larger sense, the goal of FFI Project 1394 is the development of methodology required for production CT-Analyst's underlying CFD data, comprising 18 simulations of local wind based on different meteorological wind directions. All the simulations are subject to the same data requirements and methodology, and the simulations must obviously cover (at least in part) a common geographical area.

For each simulation, the primary quantities of interest are the mean and root-mean-square velocity fields in a 14.5 × 11 = 160 km^2 area of Oslo, shown in Figure 6.1. Additionally, scalar dispersion data will be evaluated for selected wind directions and release locations, required to calibrate CT-Analyst, but this will be discussed further in a separate, future report.

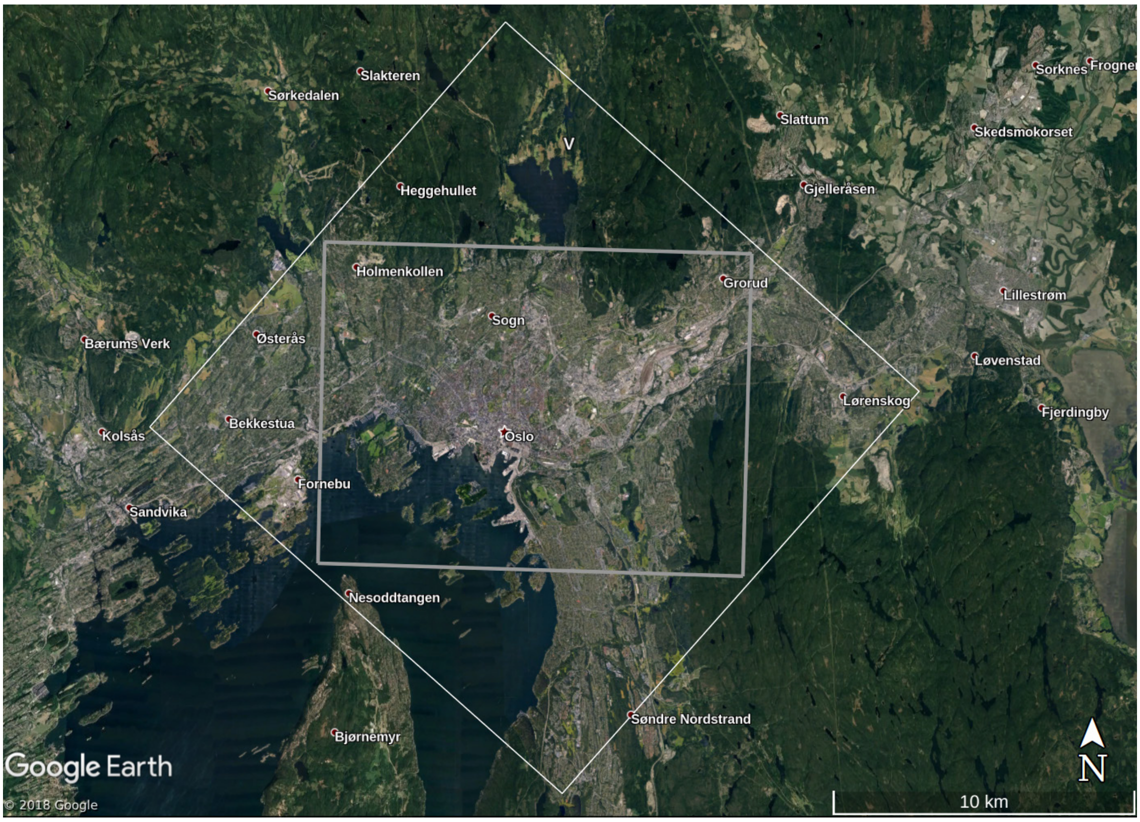

Figure 6.1 The geographical area of interest, shown as a grey rectangle in Google Earth. The dimensions of the area are 14.5 × 11 km^2. The larger white rectangle shows the computational domain for the 40° meteorological-wind simulation.

Even though the 160 km^2 geographical area of interest is the same for all simulations, the actual computational domain may be larger than this for a given simulation, depending on the meteorological wind direction simulated; to ensure similar boundary conditions in each simulation, the computational bounding box is always rotated to align with the free-stream wind. Figure 6.1 exemplifies this by illustrating the full domain for the 40° (approximately northeasterly) wind simulation in addition to the actual area of interest.

Only the region inside the 160 km^2 area of interest contains building geometry. The regions outside the area of interest (but within the computational boundary) contain only topography.[5] The computational domain of the 40° simulation is shown in Figure 6.2 as an example. The UTM lower-left and upper-right corner coordinates of the area of interest are (591704, 6638414) and (606194, 6649404), respectively.

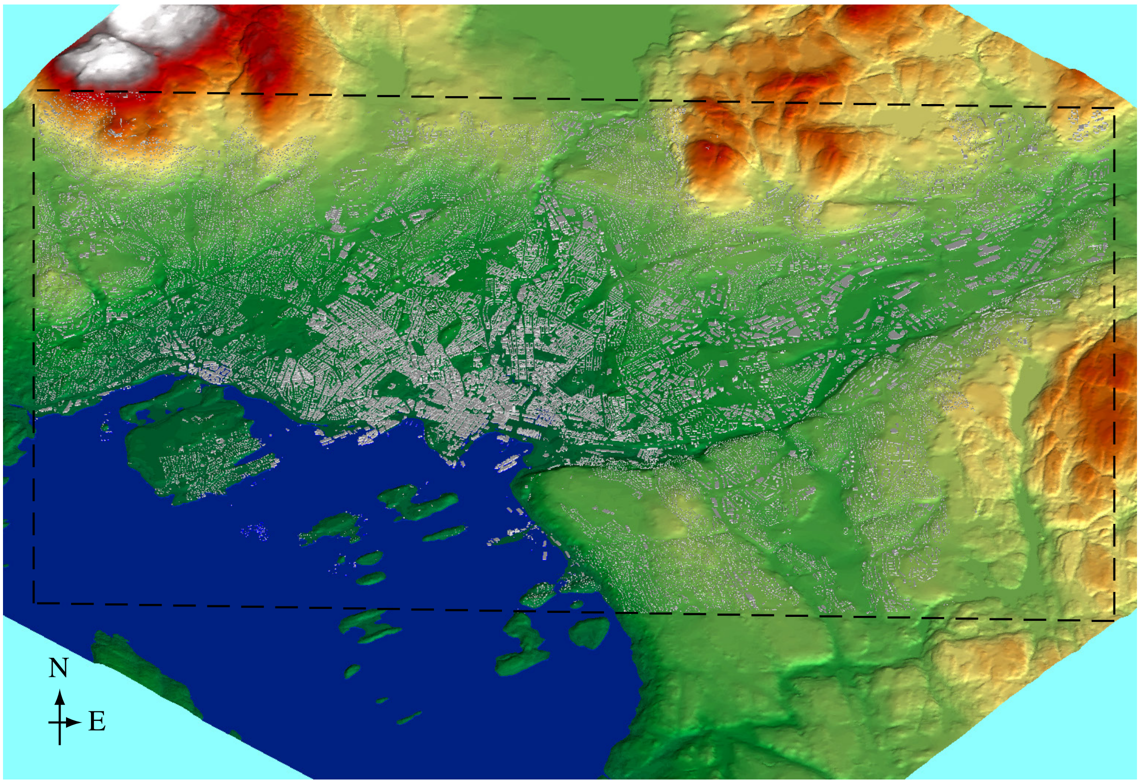

Figure 6.2 *The bottom surface (topography and buildings) of the computational domain used in the simulations with 40° and 220° meteorological wind. Topography is colored by elevation, buildings are shown in gray. Dashed lines mark the boundaries of the 160 km^2 built-up region of interest. Flow enters the domain perpendicularly to the top-right and bottom-left edges for the 40° and 220° simulations, respectively.*

In any CFD simulation, a balance between quality and performance must be found, often via an iterative trial-and-error process to investigate the sensitivity of the results to different parameters. Particularly in the present case of a very large urban area with lots of details, performance is a critical issue. Contrary to other CFD applications of urban flow, in which a predetermined smaller area is of interest (e.g., a given building or city district) and can be finely resolved at the expense of the surrounding domain, the entire 160 km^2 area of Oslo needs to be adequately resolved for input to CT-Analyst.

Consequently, the effect of the following simulation parameters on the mean and root-mean-square velocity fields have been investigated prior to the final simulations to determine the appropriate balance between quality and performance:

- Mesh resolution, ranging from 0.5 to 8 m for the smallest cells.

---

[5] These regions also have coarser computational-mesh resolutions.

- Boundary conditions for inflow and walls.
- The height of the domain, ranging from 500 m to 10 km.

Additional parameters, such as parameters related to the LES subgrid model or the linear-equation solver, have been selected on the basis of practical availability and experience.

The final choices of mesh and simulation parameters are summarized in the end of this chapter. First, the parameter sensitivity analyses will be discussed.

6.2 Mesh resolution

To compare results from urban CFD simulations thoroughly, a range of data should be investigated via different metrics, see e.g., Hertwig et al. (2017a,b) for many examples. Such rigor is, however, outside the scope of Project 1394. Instead, practical aspects and literature recommendations have been the primary bases for determining mesh resolution.

That said, several simulations have been run with different meshes, as listed in Table 6.1, to establish a sense of accuracy and performance for the different resolutions. Computational-cell growth rates, nominal maximum edge lengths and other parameters not specified in the table are common to all the mesh-study simulations and are listed later (Table 6.7) in Section 6.8.

In the following, the different mesh resolutions are investigated through simulations on a subdomain of the full Oslo geometry, using only one wind direction. The results and discussions are, however, highly relevant to the larger simulations and other wind directions as well. The subdomain used for the mesh study described here is 1190×690 m^2, and the meteorological wind flows in the x-direction, i.e., directly from the west.

Table 6.1 Parameters relevant to the mesh-sensitivity investigation; ΔL_{nom} denotes the smalles permitted computational-cell edge length (nominally, i.e., before smoothing), N_{nodes} refers to the total number of mesh nodes in the selected subdomain, and T^* is the CPU core-time spent to generate T_{stat} = 50 minutes of statistics.

Case	ΔL_{nom} [m]	N_{nodes} [1]	$T^*/10^4$ [core·s/T_{stat}]
0.5m	0.5	5,899,206	1600
1m	1	2,141,399	500
2m	2	922,951	100
4m	4	315,549	15
6m	6	178,918	6
8m	8	112,822	1

All cases in Table 6.1 have been run with the same laminar power-law inflow profile (see Section 6.4 for details), with a free-stream velocity of $U_{\text{free}} = (5, 0, 0)$. Case '0.5m' denotes the finest resolution investigated, whereas case '1m' corresponds to what is usually the recommended resolution (for the area of interest) in existing literature (cf. e.g. Tominaga et al., 2008; Xie and Castro, 2009; Franke et al., 2011). Since the Oslo geometry is very large and it is not known *a priori* which area needs particularly high resolution,[6] a coarser resolution must be accepted in the

---

[6] Indeed, *all* areas within the region of interest must have acceptable resolutions, and so it follows that, given current computational resources, no single selected area can have particularly high resolution at the expense of the rest of the domain.

Oslo simulations. All results of the mesh-study simulations are based on 50-minute statistics.

As can be seen from Table 6.1, the computational time increases drastically for increasing resolutions, as can be expected; case '0.5m' requires more than 1600 times the computational time for case '8m'.[7] This is not only due to an increasing number of mesh points; as the spatial resolution increases, the required temporal resolution also increases.

Figure 6.3 shows four locations, for which vertical profiles of mean and root-mean-square (RMS) velocites (U_i and $u_{i,\text{RMS}} = \sqrt{r_{\alpha\alpha}}$, respectively without summation on $\alpha = 1, 2, 3$, cf. Section 4.2) are shown in Figure 6.4 and Figure 6.5, respectively. The locations include two different street canyons (A and C), an open intersection (B) and a relatively open area upwind of a complex building (D).

Figure 6.3 A portion of the mesh-study subdomain, along with the locations (shown as red dots) of the vertical profiles (A-D) shown in Figure 6.4 and Figure 6.5.

Even though there is considerable variation in the vertical profiles between different locations, velocity components and resolutions, some general trends are evident.

For the mean velocity profiles, the '0.5m', '1m', and '2m' cases are largely quite similar, suggesting a convergence toward appropriate mesh resolutions, in line with literature recommendations. The '4m' case is usually closer to the finer cases than to the coarser cases, indicating that this resolution might be acceptable, although far from optimal. Contrary to the coarser cases, the '4m' case captures most of the features of the fine-resolution cases regarding sign and sign of the derivative. Particularly for the dominating velocity component (usually in the x-direction), the '4m', '2m', '1m', and '0.5m' profiles tend to align.

---

[7] The T^* values of Table 6.1 are highly approximate, as most FVM linear-equation solvers do not scale linearly with respect to either computer nodes or mesh nodes.

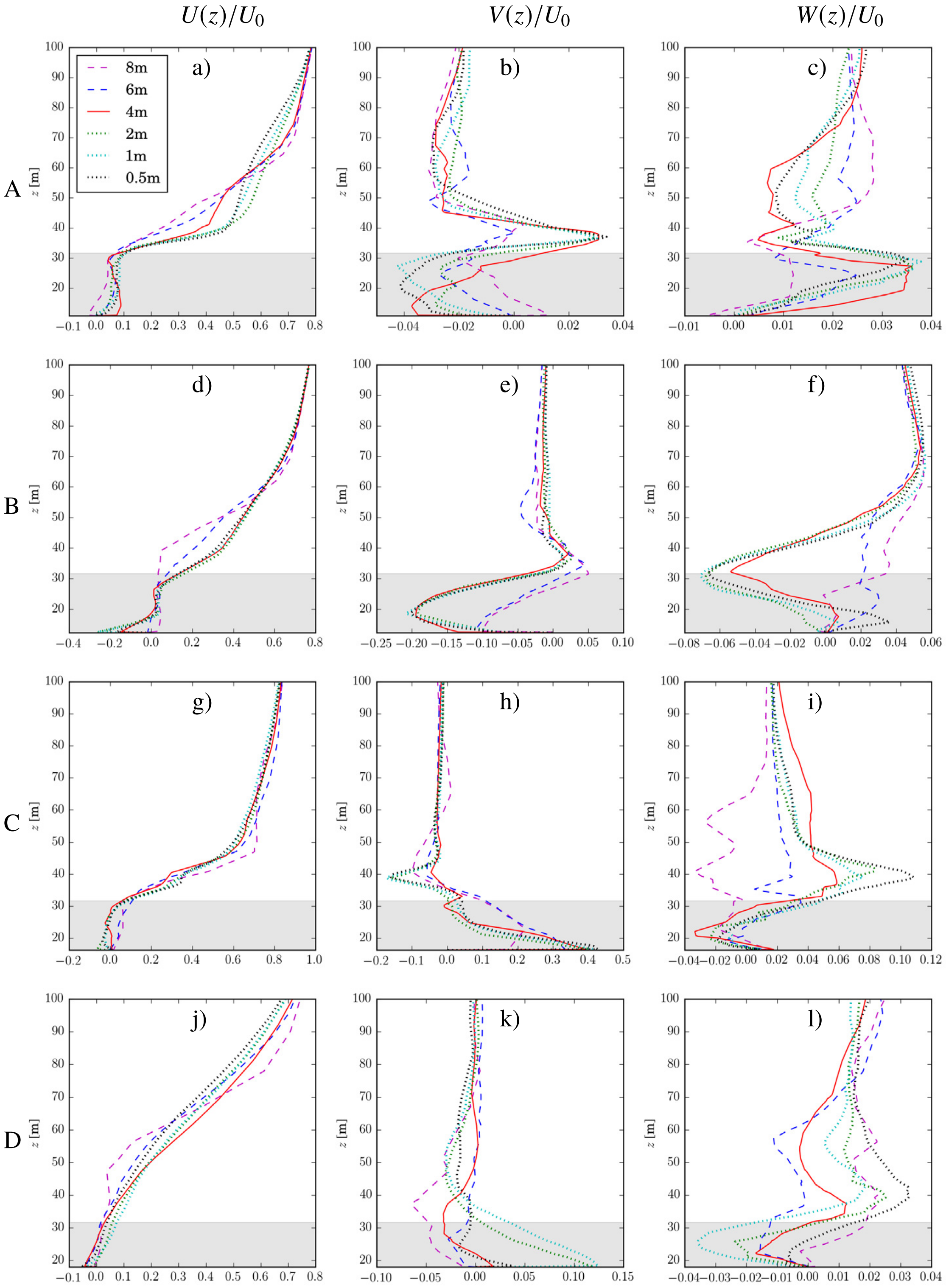

Figure 6.4 *Normalized vertical profiles of mean velocity components,* U_i/U_0*, with* $U_0 = 5.0$*, in the* x *(left column),* y *(middle column), and* z *(right columns) directions, at probe locations A (a-c), B (d-f), C (g-i), and D (j-l), ref. Figure 6.3. Profiles from cases '0.5m' through '8m', ref. Table 6.1, are shown; as indicated by the legend in subfigure 'a)', a solid, red line (——) denotes the chosen resolution ('4m'), whereas dashed (– – –) and dotted (⋯⋯) lines represent coarser and finer resolutions, respectively. The shaded area indicates the average building height within the subdomain.*

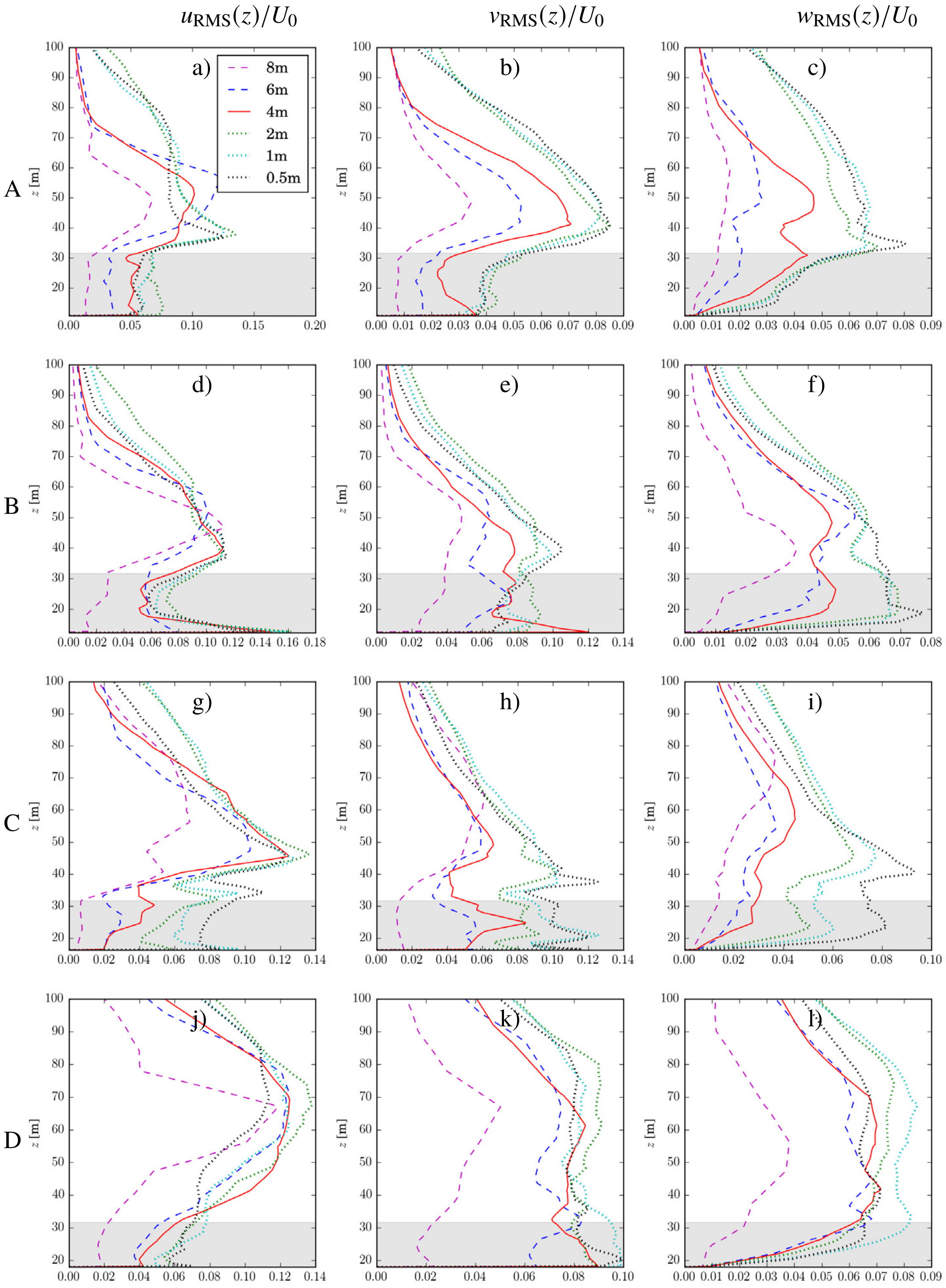

Figure 6.5 *Normalized vertical profiles of RMS velocity components, $u_{i,\mathrm{RMS}}/U_0$, with $U_0 = 5.0$, in the x (left column), y (middle column), and z (right columns) directions, at probe locations A (a-c), B (d-f), C (g-i), and D (j-l), ref. Figure 6.3. Profiles from cases '0.5m' through '8m', ref. Table 6.1, are shown; as indicated by the legend in subfigure 'a)', a solid, red line (——) denotes the chosen resolution ('4m'), whereas dashed (– – –) and dotted (⋯⋯) lines represent coarser and finer resolutions, respectively. The shaded area indicates the average building height within the subdomain.*

The RMS velocity profiles show a similar pattern, in which the ‘4m’ case lies between the coarser and finer cases quite consistently. There is a general trend that higher mesh resolution yields larger RMS values, but the differences between successively finer meshes seem to decrease towards the finer cases, as in the case of the mean velocity profiles.

For large portions of certain profiles, the ‘0.5m’ case seems to be closer to the ‘4m’ case than to the finer ‘2m’ and ‘1m’ cases, e.g., in Figure 6.4f or Figure 6.5l. The fact that the change between successive resolutions is not always monotonous can be attributed mainly to the complex flow patterns arising from the interaction of multiple jets, vortices, recirculations and so forth, whose relative strengths may not remain the same under successive refinement. The lack of perfect statistical convergence may also play a role, particuarly in the case of the RMS profiles.

On the basis of the above discussions it appears that, given the considerable computational requirements of the finer resolutions, the resolution of case ‘4m’ can be used for the 160 km^2 Oslo simulations, although a higher resolution would be preferable. Coarser meshes should be avoided. Note that the resolution of case ‘4m’ corresponds well to NRL’s commonly used (and validated in, e.g., Patnaik et al., 2009) resolutions when generating their data for CT-Analyst.

6.2.1 Comparative metrics

The data analysis in the preceding section was based on the flow details in a few selected locations in the computational domain, thereby illustrating the typical level of local agreement between different test cases. In the following, the analysis will be extended to a more quantitative comparison using appropriate validation metrics, thus enabling an assessment of the agreement between different cases on a macroscopic level.

From the large number of quantitative metrics available to compare pairs of data (cf. e.g. Oberkampf and Trucano, 2002; Britter and Schatzmann, 2007; Hanna and Chang, 2012), four common methods have been selected. Using each of these metrics, a broader assessment of the overall differences between the simulations in Table 6.1 can be made. Both the mesh convergence, i.e., the differences between successive mesh refinements, and the differences between various mesh resolutions compared to the ‘0.5m’ case as a reference case will be investigated.

For all four metrics considered in the following, data is selected from a uniform point distribution of value pairs within the area shown in Figure 6.6, from height $z = 0$ to $z = 100$ m. The selected area of interrogation begins 400 m downstream of the inlet. The points are spaced 4 m apart, and points for which the absolute value of the data falls below $u_{\text{crit}} = 0.005U_0 = 0.025$ m/s (including points “inside” buildings or below the ground surface) are removed from the data set.

The reported results are not very sensitive to the selected threshold value of u_{crit}. For the present value of u_{crit}, 167,313 value pairs or more were used in all calculated metrics.

The metrics have only been used to evaluate the performance of different mesh resolutions relative to each other. Ideally, high-quality experimental data should serve as the reference case, but this is beyond the scope of the present project. Additionally, only flow field data is used in the comparisons, as these are the fields of relevance to CT-Analyst. A later report will extend the quantitative analysis to scalar fields as well, in order to evaluate the effects of mesh resolution on simulated gas dispersion.

Figure 6.6 The area over which metrics are calculated based on a uniform distribution of interrogation points is shown in red. The full urban area of the simulations used for parameter investigations is shown in gray. The global wind direction is from left (west) to right.

6.2.1.1 Factor of two (FAC2)

The FAC2 metric measures how large a portion of the included value pairs comprise values that fall within a factor two of each other, i.e.

$$\mathrm{FAC2} = \frac{1}{N}\sum_i F_i, \quad \text{with} \quad F_i = \begin{cases} 1 & \text{if } \frac{1}{2} \leq \frac{C_{t,i}}{C_{r,i}} \leq 2, \\ 0 & \text{otherwise,} \end{cases}$$

where C_t denotes the test data, C_r is the reference data, and N is the number of value pairs. Note that FAC2 is symmetric with respect to the test and reference data, and that it is bounded in $[0, 1]$.

FAC2 measures the bulk performance of the test data, particularly while maintaining a certain robustness to rare, strong over- or underpredictions. For flow and dispersion studies in urban areas, a threshold value of FAC2 = 0.5 is sometimes recommended as a binary classification of the model into sufficient or insufficient predictive quality (Hanna et al., 2004; Hertwig et al., 2017a) when comparing predictions to observations, though this is not necessarily as relevant a criterion when comparing different mesh resolutions.

Table 6.2 presents the FAC2 validation metric for the mean and RMS velocity fields, as well as the velocity magnitude. The table is divided into two sections, corresponding to the mesh-convergence check and the comparisons to the refence case (‘0.5m’).

There are evident trends visible in Table 6.2. It is clear that the velocity magnitude, $|U_i|$, is most robust to changes in mesh resolution, most likely stemming from the fact that directional information is absent from this quantity. The streamwise velocity component also performs rather well across all comparisons. On the other hand, the velocity fluctuations are the most sensitive data, rapidly deteriorating for low mesh resolutions.

In terms of mesh convergence, there is a monotonous trend towards better agreement as the resolution is successively increased, which is a strong implication of mesh convergence (at least for the statistics under consideration). When doubling the resolution from 2 m to 1 m, more than 90 %

Table 6.2 Factor of two (FAC2) ratios for different case pairs. Case notations correspond to Table 6.1.

Case pair	U	V	W	$\lvert U_i \rvert$	u_{RMS}	v_{RMS}	w_{RMS}
Mesh convergence							
8m vs. 4m	0.905	0.656	0.725	0.929	0.547	0.531	0.488
4m vs. 2m	0.959	0.802	0.830	0.977	0.815	0.849	0.812
2m vs. 1m	0.985	0.917	0.937	0.994	0.999	0.999	0.998
1m vs. 0.5m	0.982	0.919	0.941	0.994	0.992	1.000	0.998
Validation against "reference"							
8m vs. 0.5m	0.874	0.588	0.685	0.901	0.455	0.382	0.282
6m vs. 0.5m	0.918	0.707	0.750	0.942	0.748	0.659	0.499
4m vs. 0.5m	0.947	0.777	0.811	0.968	0.862	0.868	0.777
2m vs. 0.5m	0.975	0.863	0.900	0.989	0.949	0.983	0.967
1m vs. 0.5m	0.982	0.919	0.941	0.994	0.992	1.000	0.998

of the value pairs comprise values within a factor two of each other.

When validating different resolutions against the '0.5m' reference, it is seen that the '8m' resolution is insufficient; all fluctuating fields have less than half their value pairs within the FAC2 criterion. The '6m' case show improvement, but w_{RMS} still has a FAC2 measure of 0.474. Significant improvement is found when comparing '4m' to '0.5m'; the FAC2 metric lies around 0.8 or higher. This indication of sufficient quality corresponds nicely to the previous discussion regarding the vertical profiles in Figure 6.5. Unsurprisingly, the '2m' and '1m' cases show even better agreement.

6.2.1.2 Modified normalized mean bias (MNMB)

The MNMB is a measure of the degree of systematic over- or underprediction of a test data set relative to a reference data set, and it is given by

$$\mathrm{MNMB} = \frac{2}{N} \sum_{i=1}^{N} \left(\frac{C_{t,i} - C_{r,i}}{C_{t,i} + C_{r,i}} \right),$$

where $C_{t,i}$ denotes the test data, $C_{r,i}$ is the reference data, and N is the number of value pairs. Note also that the MNMB can be related to equivalent consistent relative under-/overprediction of data via simple algebra, cf. Appendix A.

The MNMB metric has a range of $[-2, 2]$, in which zero is the optimal result (i.e., no bias), and it can only be used with data fields which have strictly positive or strictly negative values. The metric is therefore only given for the mean velocity magnitude and the RMS velocities when listed in Table 6.3.

Unsurprisingly, the trends in Table 6.3 correspond well to those in the FAC2 metrics of Table 6.2, and the conclusions will not be repeated here. However, the degrees and directions of bias shown in the MNMB table provides additional insight.

It is clear that coarser mesh resolutions generally result in systematic *under*prediction of velocities, particularly velocity fluctuations, relative to the fine '0.5m' case. For the '4m' resolution the fluctuating-velocity bias is roughly between -0.30 and -0.45, corresponding to a systematic

Table 6.3 Modified normalized mean biases (MNMB) for different case pairs. Case notations correspond to Table 6.1.

Case pair	$\lvert U_i \rvert$	u_{RMS}	v_{RMS}	w_{RMS}
Mesh convergence				
8m vs. 4m	-0.076	-0.570	-0.537	-0.597
4m vs. 2m	-0.028	-0.329	-0.375	-0.429
2m vs. 1m	-0.008	0.045	0.012	-0.010
1m vs. 0.5m	0.004	0.095	0.068	0.030
Validation against "reference"				
8m vs. 0.5m	-0.103	-0.727	-0.772	-0.912
6m vs. 0.5m	-0.059	-0.333	-0.474	-0.613
4m vs. 0.5m	-0.030	-0.214	-0.311	-0.419
2m vs. 0.5m	-0.004	0.137	0.077	0.020
1m vs. 0.5m	0.004	0.095	0.068	0.030

underprediction of between 26 % and 37 %, cf. Appendix A. The mean velocity magnitude is reasonably well predicted in the '4m' case relative to the '0.5m' case.

6.2.1.3 Fractional gross error (FGE)

The FGE measures the mean absolute error of a test data set compared to reference data (or vice versa; the FGE is symmetric), and as for the MNMB, only strictly positive or strictly negative data fields are admittable. The FGE has a range of $[0, 2]$, in which zero is the best result (no errors). The metric is calculated as

$$\mathrm{FGE} = \frac{2}{N} \sum_i \left| \frac{C_{t,i} - C_{r,i}}{C_{t,i} + C_{r,i}} \right|,$$

Note that it is always the case that $\mathrm{FGE} \geq \mathrm{MNMB}$. Thus, if $\mathrm{MNMB} \neq 0$, then also $\mathrm{FGE} \neq 0$, but the reverse is not necessarily true; a test data set with no systematic bias may still have random scatter compared to the reference data, thus yielding a nonzero FGE. The special case of FGE = MNMB indicates that all the errors in the test data are systematic.

Table 6.4 lists the FGE for a selection of case pairs. Again, the general trends in the metrics correspond nicely to the metrics considered in previous subsections and will not be discussed in more detail here. It is, however, relevant to assess the FGE metric for certain case pairs, particularly in combination with the MNMB metric.

When comparing the '4m' to the '0.5m' case, the FGE for the velocity magnitude is three times the magnitude of the MNMB, suggesting that random errors are more significant than the systematic underprediction, which is around about 3 %. For the velocity fluctuations, on the other hands, the two metrics are comparable, indicating that while there is some scatter in the compared data, most of the errors are due to the systematic bias.

6.2.1.4 Correlation coefficient (R)

The linear correlation coefficient, R, measures the degree of common variation in two data sets, thus favoring the correlation of (one-point) statistical trends instead of a comparison of absolute

Table 6.4 Fractional gross errors (FGE) for different case pairs. Case notations correspond to Table 6.1.

Case pair	$\lvert U_i \rvert$	u_{RMS}	v_{RMS}	w_{RMS}
Mesh convergence				
8m vs. 4m	0.192	0.662	0.693	0.710
4m vs. 2m	0.112	0.362	0.385	0.436
2m vs. 1m	0.057	0.129	0.105	0.129
1m vs. 0.5m	0.057	0.140	0.114	0.117
Validation against "reference"				
8m vs. 0.5m	0.235	0.770	0.852	0.947
6m vs. 0.5m	0.172	0.434	0.528	0.652
4m vs. 0.5m	0.126	0.319	0.352	0.440
2m vs. 0.5m	0.077	0.200	0.170	0.186
1m vs. 0.5m	0.057	0.140	0.114	0.117

data values. The correlation coefficient is symmetric and defined as

$$R = \frac{\frac{1}{N}\sum_i (C_{t,i} - \langle C_t \rangle)(C_{r,i} - \langle C_r \rangle)}{\sigma_t \sigma_r},$$

in which $\langle C_t \rangle$ and $\langle C_r \rangle$ are the averages over all points in the test and reference data sets, respectively, and σ_t and σ_r are the standard deviations of the same data sets. R ranges from -1 to 1, where 0 signifies no correlation and 1 and -1 implies full correlation and full anti-correlation, respectively.

Table 6.5 summarizes the results of the R metric for selected case pairs. Similar trends exist as for the other metrics; the correlation coefficients generally tend to show better agreement across all case comparisons. This corroborates both the indications of the vertical profiles in earlier subsections as well as the relatively dominating systematic bias compared to random differences between data sets.

For the '4m' case, the correlation with the '0.5m' reference is typically around 0.9 or higher, indicating that the two simulations display very similar statistical trends.

6.2.1.5 Concluding remarks on comparative metrics

In conclusion, the quantitative metrics all suggest that for the coarsest meshes ('8m' and '6m'), there is both a systematic underprediction as well as significant random errors. The trends are somewhat correlated to the reference data, but relatively few values are within a factor two of the reference values. This indicates that the '8m' and '6m' cases fail to capture the relevant physics to a sufficient degree.

For the selected resolution, '4m', the main problem is systematic underprediction of fluctuating velocities relative to the '0.5m' case. This bias virtually disappears in the '1m' and '2m' cases, although some random scatter compared to the reference case still persists. The mean velocity fields are generally in acceptable agreement with the '0.5m' case for both the '4m', '2m' and '1m' cases. In summary, the '4m' case seem to represent at least the most significant flow physics reasonably well.

Table 6.5 Correlation coefficients (R) for different case pairs. Case notations correspond to Table 6.1.

Case pair	U	V	W	$\lvert U_i \rvert$	u_{RMS}	v_{RMS}	w_{RMS}
Mesh convergence							
8m vs. 4m	0.958	0.803	0.831	0.954	0.656	0.526	0.539
4m vs. 2m	0.986	0.923	0.923	0.984	0.882	0.913	0.897
2m vs. 1m	0.996	0.973	0.971	0.995	0.959	0.971	0.956
1m vs. 0.5m	0.996	0.973	0.975	0.995	0.966	0.974	0.961
Validation against "reference"							
8m vs. 0.5m	0.943	0.729	0.760	0.939	0.555	0.399	0.349
6m vs. 0.5m	0.971	0.829	0.830	0.968	0.776	0.725	0.633
4m vs. 0.5m	0.983	0.894	0.898	0.981	0.856	0.853	0.799
2m vs. 0.5m	0.993	0.952	0.951	0.992	0.931	0.937	0.897
1m vs. 0.5m	0.996	0.973	0.975	0.995	0.966	0.974	0.961

These conclusions are well in line with the implications from the vertical profiles considered earlier, cf. Section 6.2. A refinement in mesh resolution from the '4m' to the '2m' case would cause considerable quality improvement while still remaining much cheaper than the '1m' or '0.5m' cases in terms of computational requirements. However, given the available computational resources compared to the number and size of simulations, the '4m' resolution is deemed sufficient *for the intended use of the results* at this point. That said, care should be taken when assessing the turbulence levels based on the '4m' resolution, as an underprediction of roughly 30 % can be expected.

Figure 6.7 shows that, indeed, for CT-Analyst, the '4m' case seems to capture the most important mean-flow effects of the urban environment, such as local recirculation regions and the mean flow directions.[8] However, based on the results discussed above, turbulence kinetic energy can be expected to be somewhat underpredicted relative to the finer resolutions.

For other applications than CT-Analyst, such as wind-load computations or turbulence-intensity estimates of interest to drone flight, the selected resolution of case '4m' might not suffice. Similarly, for scalar-transport simulations requiring high fidelity, a higher required resolution can be expected. A future report will discuss similar metrics as shown here for scalar-dispersion simulation results.

For smaller domains or a smaller range of simulated global-wind directions than is needed for CT-Analyst, the mesh resolution should be refined to at least the level of case '2m' whenever possible. An example of such a more finely resolved simulation at FFI can be found in Fossum and Helgeland (2019).

Finally, it should be mentioned that in CT-Analyst, the effect of turbulent mixing can be scaled (globally) to account for any systematic under- or overprediction in the CFD data, if known.

---

[8] Turbulence-level contours are not shown here, but display similar trends, though with lower turbulence kinetic energy values in the '4m' case.

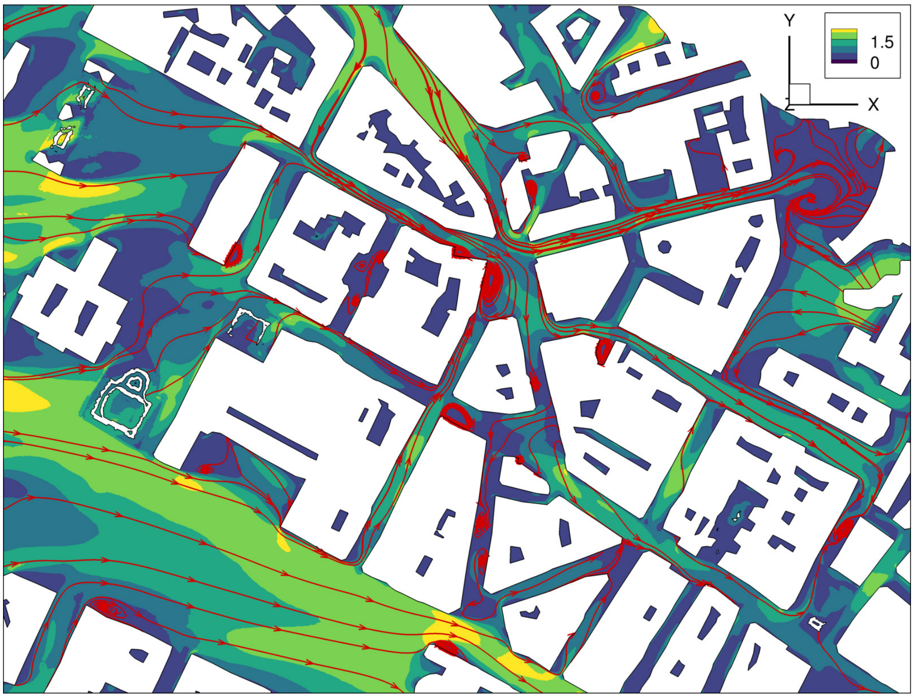

(a) Case ‘0.5m’.

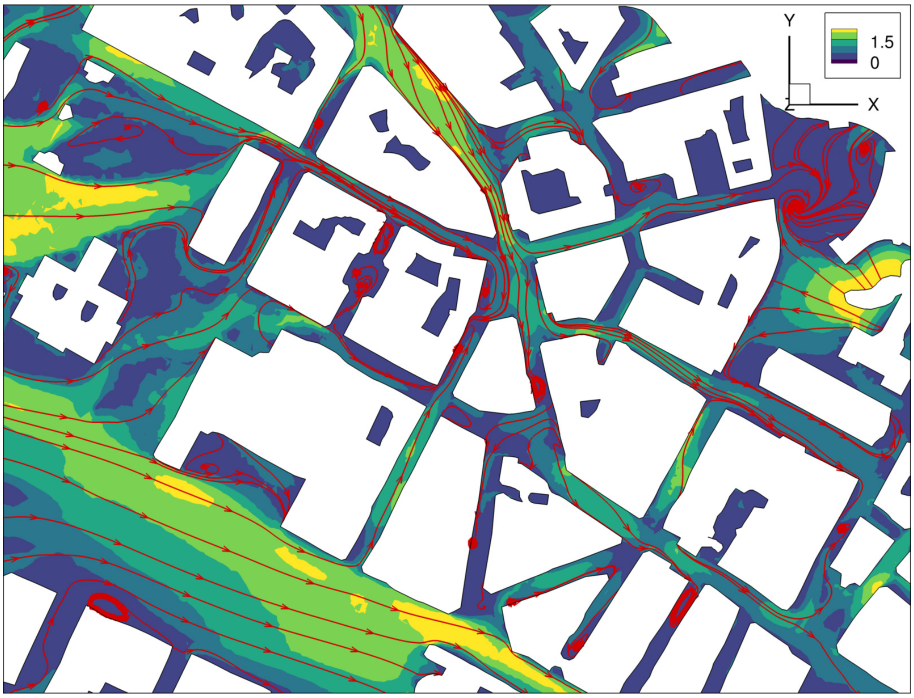

(b) Case ‘4m’.

Figure 6.7 Streamlines of mean horizontal flow (in red) overlaid on contour plots of mean horizontal velocity magnitudes ($\sqrt{U^2 + V^2}$) in a cutplane at $z = 20$ m for two of the cases in Table 6.1.

6.3 Solid-wall boundary conditions

Solid surfaces, such as the ground and building walls in urban CFD simulations, can be modeled as walls with various degrees of slip. For a strongly imposed no-slip condition, all computational nodes at walls are simply specified to have zero velocity, whereas in the case of full slip, only the normal velocity is explicitly set to zero, and the wall-tangential velocity is depends fully on the outer flow. In-between these two extremes, various partial-slip models exist, which will not be discussed here.

The no-slip condition can, however, also be weakly imposed via a so-called penalty condition. In that case, the mesh nodes at the walls are not explicitly set to zero. Instead, a momentum flux is introduced at the boundary nodes in order to dynamically reduce the velocity towards zero when solving the set of linear equations.

There are few comparisons of the two no-slip formulations, particularly for finite-volume methods. Bazilevs and Hughes (2007) argue in favor of the weak formulation, and shows convincing results in a finite-element context. There are also intuitive arguments for using the weak approach in the case of urban CFD; wall-adjacent computational nodes are less affected by the no-slip condition in a weak formulation, which seems particularly suitable for coarse meshes (relative to the viscous scales). Also, narrow streets might be resolved with merely four or five cells across, in which case viscous forces from the side walls may artificially impede the flow to a larger degree in the strong formulation.

That said, the strong formulation is widely used, it seems intuitive, and the notion of actual zero velocity on walls resonate well with physical intuition. Besides, the weak formulation is slightly less numerically stable in CDP.

Figure 6.8 shows selected profiles from location A in Figure 6.3. These figures are representative of similar data at other locations and show that, indeed, the ‘4m’ case with weak no-slip formulation does seem to compare better to the “reference” case (i.e., ‘1m’) than the corresponding strongly formulated no-slip ‘4m’ simulation. The figures also show that the ’1m’ case with strong conditions agrees well with the weak-condition ’1m’ case. This is expected, as the effect of how the boundary condition is formulated should diminish with mesh resolution.

The data exemplified in Figure 6.8 is corroborated further by the metrics in Table 6.6. In the table, quantitative comparisons between coarse (’4m’) and fine (’1m’) simulations are evaluated using the four metrics from Section 6.2. Within each comparison, the same boundary-condition formulation is used for the fine and coarse simulations. Thus, the coarse simulation will not be compared to a “reference” with a different boundary-condition formulation. Rather, the reduction in quality as a function of mesh coarsening for a given formulation is isolated from the particular choice of formulation. That said, as seen both in Figure 6.8 and from a quantitative comparison (not shown), the ’1m’ cases are generally quite similar for the two boundary-condition formulations.

From Table 6.6, it is clear that for every single metric and every applicable flow field, the coarsely resolved weak boundary-condition formulation perform better than its strongly formulated counterpart when compared to finely resolved simulations of similar formulations.

In conclusion, the weakly formulated no-slip boundary condition seems to perform better than the strong formulation. This is thus what has been used in the simulations documented in this report.

As a final remark, it should be noted that in previous versions of CT-Analyst Oslo, the CFD data was based on simulations where the strong no-slip condition was enforced. This was due to stability issues with older versions of CDP and will be changed in future versions of CT-Analyst.

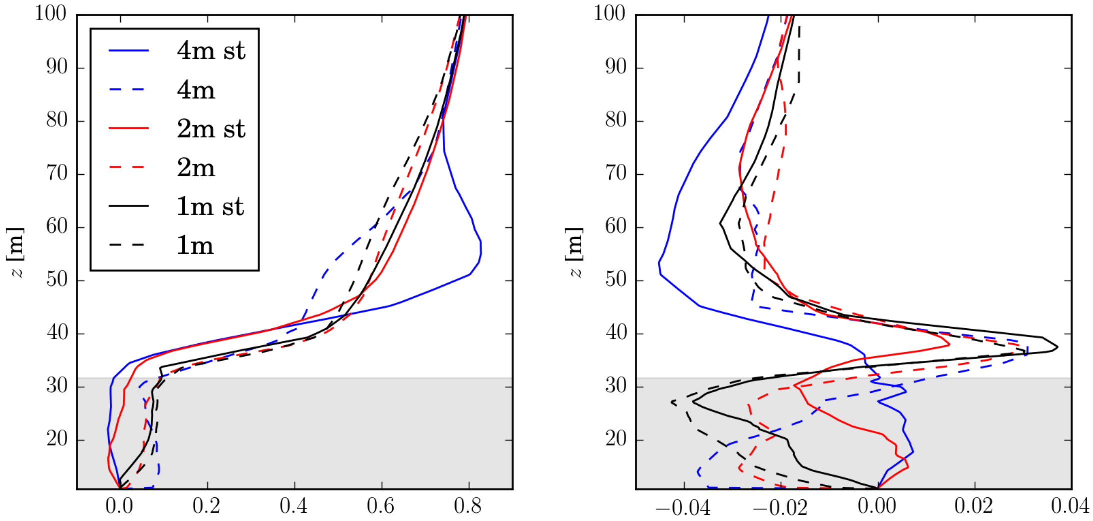

(a) $U(z)$.

(b) $V(z)$.

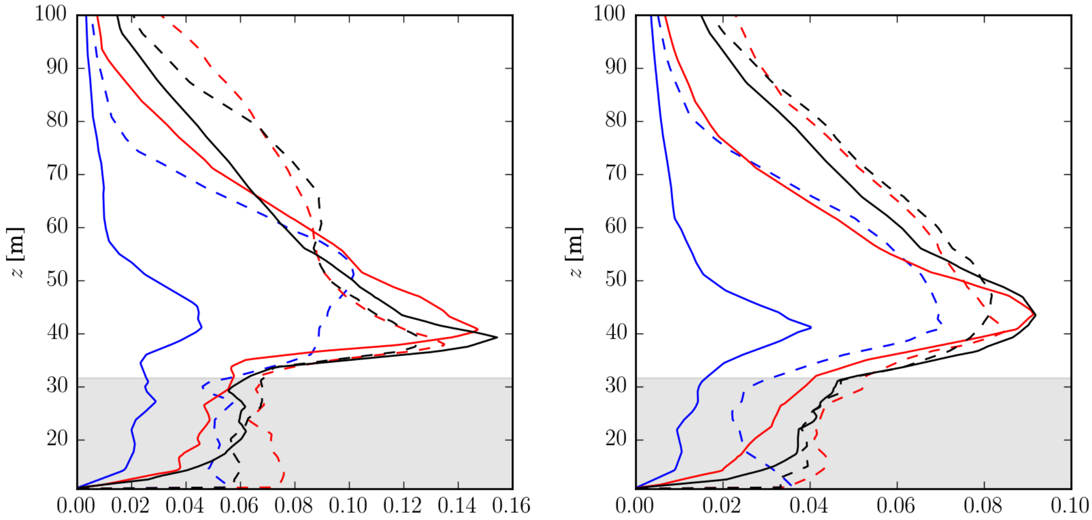

(c) $u_{\mathrm{RMS}}(z)$.

(d) $v_{\mathrm{RMS}}(z)$.

Figure 6.8 *Normalized vertical profiles of selected mean and RMS velocity components,* U_i/U_0 *and* $u_{i,RMS}/U_0$*, respectively, with* $U_0 = 5.0$*, at probe location A, ref. Figure 6.3. Profiles from cases '1m' (black), '2m' (red), and '4m' (blue), ref. Table 6.1, are shown using both weakly and strongly formulated wall boundary conditions; as indicated by the legend in the top left figure, solid lines (——) denote the strong-condition simulations, whereas dashed (−−−) lines represent weak-condition simulations. The shaded area indicates the average building height within the subdomain.*

Table 6.6 Selected comparative metrics for '1m' and '4m' case pairs with strongly and weakly formulated boundary conditions, respectively.

Case pair	U	V	W	$\|U_i\|$	u_{RMS}	v_{RMS}	w_{RMS}
Weakly imposed boundary condition							
FAC2	0.951	0.821	0.848	0.971	0.830	0.856	0.790
MNMB	N/A	N/A	N/A	-0.034	-0.298	-0.372	-0.446
FGE	N/A	N/A	N/A	0.117	0.341	0.383	0.452
R	0.987	0.906	0.915	0.985	0.888	0.894	0.868
Strongly imposed boundary condition							
FAC2	0.886	0.629	0.719	0.907	0.663	0.628	0.604
MNMB	N/A	N/A	N/A	-0.076	-0.446	-0.551	-0.569
FGE	N/A	N/A	N/A	0.230	0.529	0.573	0.599
R	0.957	0.750	0.801	0.954	0.751	0.757	0.707

6.4 Inflow boundary conditions

In general, the inflow boundary conditions can be critical to the flow features in the interior of a computational domain, as the features from the inlet can be advected downstream almost unaltered for a distance of many boundary-layer thicknesses.

That said, for fluid flow in more heterogeneous geometries, with many obstacles or high roughness, local dynamics may rapidly dominate the flow evolution in affected regions. In urban CFD, the urban canopy represents such a region; the urban geometry can be expected to dynamically dominate the flow, effectively rendering inflow details insignificant. However, the outer flow, i.e., the flow at higher altitudes, is still likely to depend strongly on the details of the inlet boundary conditions.

A problem concerning many real-life flows is the lack of empirical flow data at the inlet. This is also the case in atmospheric boundary-layer flow, including urban-flow simulations. It is therefore to be hoped that the exact details of the incoming boundary layer is not too significant for the flow within the urban canopy, as such details are frequently both statistically heterogeneous and seldom available in practice, due to the potential presence of large-scale weather phenomena (cf. e.g. García-Sánchez and Gorlé, 2018).

Excluding the unrealistic case of plug inflow (i.e., uniform inflow velocity), laminar and turbulent boundary-layer inflows are the two most common distinct classes of relevant inflows to an urban-flow simulation. If the differences between the interior flows within the region of interest are negligible even when comparing laminar to turbulent inflows, then the specific details of the turbulence profiles on the inflow can safely be considered unimportant.[9]

To investigate the degree to which imposed turbulence at the inflow affects mean and RMS velocity profiles within the urban area, two different boundary conditions have been imposed on the inlet. The two inflows that have been considered are as follows:

- Laminar power-law inflow with $\tilde{u}_{\mathrm{in}}(z) = U_0 Z^{\alpha}$.

---

[9] Different mean inflow profiles have not been investigated, as this profile must comply with CT-Analyst's assumption of a power-law profile.

- Turbulent inflow with power-law mean flow; $U_{\text{in}}(z) = U_0 Z^{\alpha}$.

In the above, $U_0 = 5.0$ m/s, $z_\delta = 300.0$ m, $Z = \min(z/z_\delta, 1)$, and $\alpha = 0.25$ are the free-stream velocity, boundary-layer thickness, normalized vertical coordinate, and power-law exponent, respectively.

The turbulent inflow case uses the same mean-flow profile as the laminar case, onto which turbulent fluctuations are superposed through a discrete-filtering technique in CDP. The discrete filtering ensures that the mean flow at the inflow converges to the user-specified profile over time, while introducing turbulent eddies consistent with the desired characteristic length scales. Presently, the characteristic length and velocity scales used are $L = 150$ m and $U_n = 3$ m/s, respectively.[10]

The turbulent inflow satisfies mass conservation, whereas momentum conservation is not guaranteed. Thus, as for most synthetic turbulent-inflow generators, the flow needs some time to adjust itself in the interior of the domain.

The turbulent profiles used to specify the components of the Reynolds-stress tensor, r_{ij}, in the turbulent case is given by appropriate profiles for neutral ABLs (Stull, 2017, p. 707)

$$\begin{aligned}
r_{11} &= \left(2.5u_* e^{-1.5Z}\right)^2, \\
r_{22} &= (1.6u_*(1 - 0.5Z))^2, \\
r_{33} &= (1.25u_*(1 - 0.5Z))^2, \\
r_{12} &= r_{21} = 0, \\
r_{13} &= r_{31} = 0, \\
r_{23} &= r_{32} = 0,
\end{aligned}$$

where $u_* = 0.5$ m/s is the friction velocity. The actual statistical profiles found at the synthetic-turbulence inlet will not generally correspond to the specified Reynolds-stress profiles, as the filtering process prioritizes correct mean flow, characteristic scales and coherent structures. Such lack of consistency in RMS profiles is far from ideal in many cases, but it is unproblematic here.

The computational time varies considerably less than in the case of differing mesh resolutions. The turbulent-inflow simulation generally requires between 20 % and 80 % more time than the laminar-inflow case, depending on the choice of characteristic scales; in the case used here, about 40 % more time is used.

Initially, the effects of the inflow conditions were evaluated on the same small subdomain as was used for the mesh-resolution study (cf. Section 6.2). Rather significant differences were found. However, it was also discovered that the differences between the two inflow cases decreased with distance downwind from the inflow, indicating that the small test domain might be too small for this parameter study. Consequently, the full Oslo domain is used in the inflow parameter study.

Figure 6.9 shows the entire region of interest. In the inflow study, global wind is from the north, i.e., the north boundary represents the velocity inlet. The red rectangular boxes shown in Figure 6.9 shows the five different regions over which comparative flow metrics have been calculated for the two inflows. Each rectangle is 1×1 km^2, so as to cover a large representative area of the geometry. The regions range from the ground up to 100 m above the local ground level in the vertical direction.

For each rectangular region in Figure 6.9, pairs of points from the laminar-inflow simulation and the turbulent-inflow simulation, respectively, are evaluated statistically through the metrics defined earlier (cf. Section 6.2). The points are distributed uniformly with a resolution of 4 m, and

---

[10] Other values have been investigated with only negligible effects on the resulting interior flow.

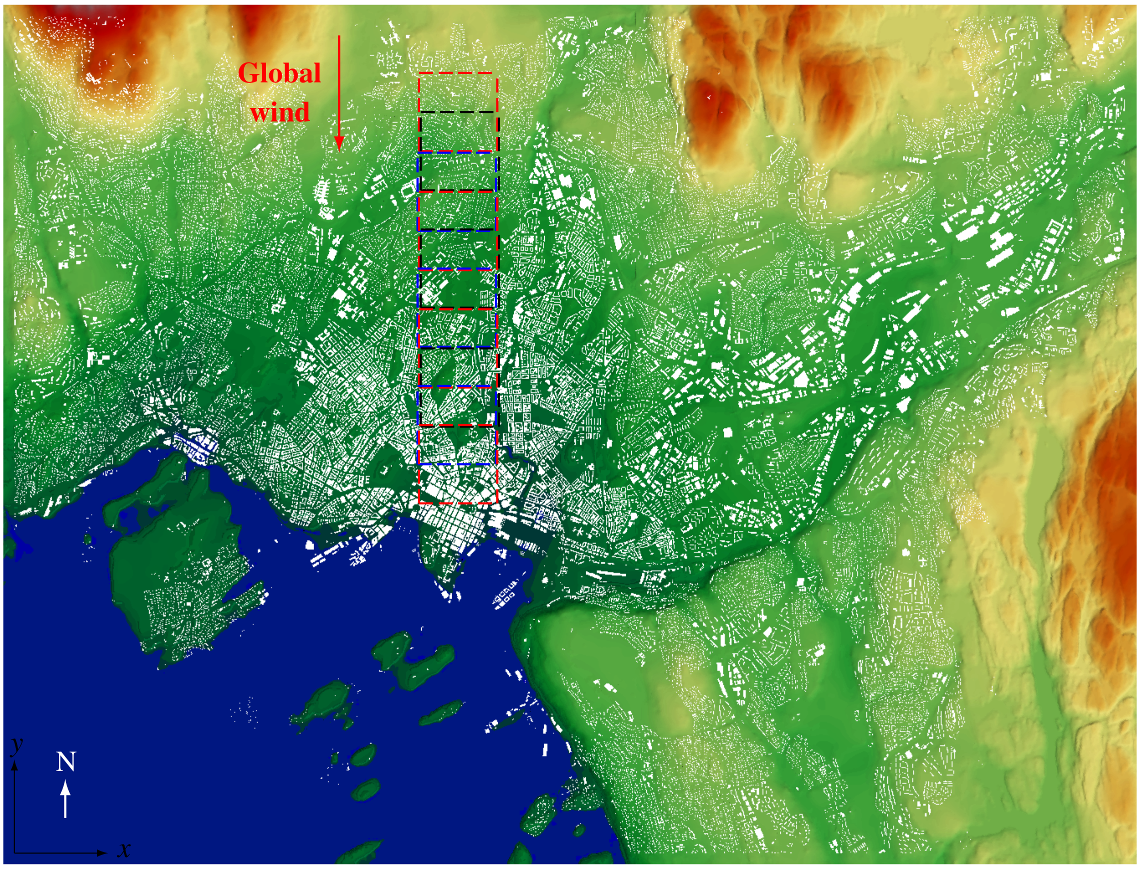

Figure 6.9 *The geometry used in the inflow-condition parameter study. The northern boundary represents the inlet. The rectangular boxes (different colors and minor relative translations used simply for clarity) show the 10 regions over which comparative metrics have been computed, moving 500 m downstream for each successive box.*

the exclusion criterion for the pointwise pairs is as defined in Section 6.2. The four metrics (FAC2, MNMB, FGE, R) thereby quantify the effects a laminar relative to a turbulent inflow have on the flow field statistics in the interior urban area.

In Figure 6.10 the four metrics are plotted for each rectangular region as functions of downwind distance. Clearly, up to a certain limit, the effects of different inflow boundary conditions seem to diminsh with distance from the inlet.

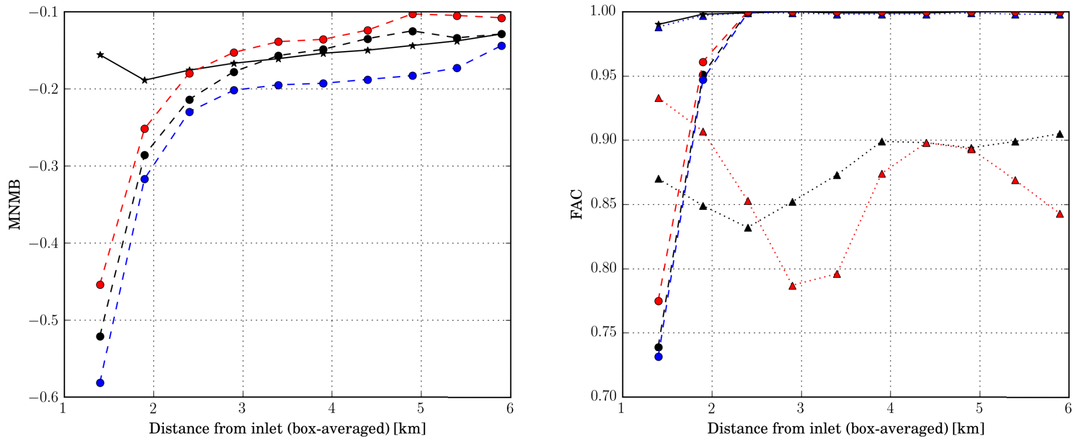

(a) Modified normalized mean bias.

(b) Factor of two.

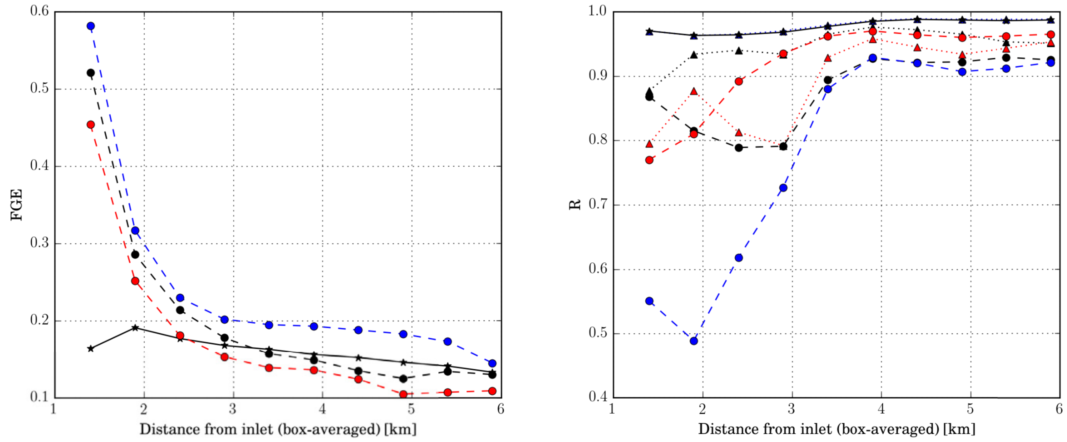

(c) Fractional gross error.

(d) Correlation coefficient.

Figure 6.10 Metrics for a pointwise comparison of interior flow fields simulated with laminar and turbulent inlets, respectively. The x-axis denotes the distance from the inlet to the centroid of each rectangular region for which metrics have been calculated (cf. Figure 6.9). Mean velocity magnitude (solid line w/stars), u_{RMS} (black, dashed line w/circles), v_{RMS} (blue, dashed line w/circles), and w_{RMS} (red, dashed line w/circles) are shown. Mean x (black, dotted line w/triangles), y (blue, dotted line w/triangles), and z (red, dotted line w/triangles) components are shown where applicable.

Generally, the MNMB improves steadily for the entire range of regions investigated, from a bias of almost -0.5 for the velocity fluctuations close to the boundary to less than -0.15 farthest from the inlet. However, the most significant improvement occurs in the first 2.5 km from the boundary, with one notable exception: The mean velocity magnitude actually displays a smaller bias closest to the inlet than for the next 3 km into the domain. Most likely, this is due to the lack of urban geometry close to the boundary, resulting in flow more dominated by the inflow conditions than for areas farther downwind. This means that the mean flow (which is equal for the two inflow conditions) will have a small bias close to the inlet, whereas the fluctuations (which are completely absent from the laminar inflow) exhibit larger biases there.

The FGE shows similar trends as the MNMB; the mean velocity magnitude remains relatively steady but with a slight improvement farther from the boundary (except from the first to the second downwind region). Again, this is unsurprising, given that the two inlets have identical mean flow profiles. The profiles for the velocity fluctuations, which are very different at the inlet, improves rapidly for the first 2 km into the domain and keeps improving at a slower rate farther downwind.

The FAC2 metric approaches unity about 2.5 km into the domain for all fields except two; the metrics for the mean transversal and vertical velocity components generally lie between 0.8 and 0.9, with no significant sign of improvement or degradation with downwind distance. This indicates that the difference might not be an effect of the difference in inflows. The reason for the (relatively) low agreement might be lack of statistical convergence or a high sensitivity of these fields to the FAC2 metric, caused by, say, the dependence on the exact location of recirculation regions.

The correlation coefficient also improves with downwind distance; at around 3.5 km, the effect of the inflow boundary has largely disappeared.

Considering all the metrics together, three main patterns emerge: Firstly, the effects of the inflow conditions on the interior flow clearly diminish with downwind distance. Secondly, the velocity fluctuations are more significantly affected by the type of inflow than is the mean flow, but the effects on the fluctuations are also more rapidly reduced downwind. Thirdly, it generally appears that within approximately 3 km from the inlet, the effects of the choice of inflow are minor.

In light of these findings, it is concluded that laminar inflow boundary conditions most likely suffice for large urban-flow simulation for which the result of main interest is ground-level wind fields. However, care must be taken close ($<$ 3 km) to the inflow boundary, as the results are more dependent on the inflow conditions there. Furthermore, for the atmospheric boundary layer, any turbulent inflow is more realistic than a laminar inflow, so a turbulent inflow will be used in the Oslo simulations. A turbulent inflow also instigates dynamic turbulence generation, caused by the urban geometry, more rapidly. The findings reported here suggest that the exact details of the turbulent profiles and characteristics are negligible on the interior urban flow.

Simulations (not shown here) of laminar and turbulent inflow profiles on finer meshes for smaller subdomains indicate that the differences between the two inflow types decrease as mesh resolution increases.

6.5 Domain height

In general, the height of the computational domain should be as large as possible in order to minimize the flow-contraction effects of topography and buildings. However, the mesh resolution can be rather coarse far from the region of interest, i.e., at higher altitudes.

The effect of topography can be roughly estimated by simple calculations. Consider a single two-dimensional hill of height H_{hill}, towards which blows a steady inviscid flow with velocity U_0, as illustrated in Figure 6.11. For a domain of height H_{dom}, the corresponding increase in wind velocity due to the contraction caused by the hill will be $U_1 = U_0 H_{\text{dom}} / (H_{\text{dom}} - H_{\text{hill}})$ at the crest of the hill, assuming inviscid and incompressible flow.

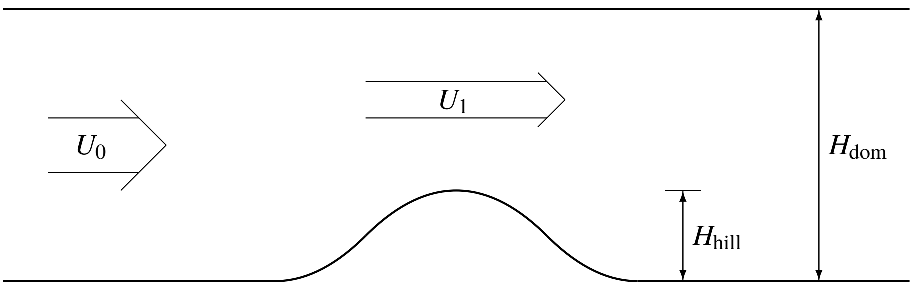

Figure 6.11 Simplified flow over a two-dimensional hill.

Now, for a hill height of 500 m, quite representative of the Oslo topography, it is easily seen that a domain height of 1 km will incur a doubling of the wind velocity over the hill, i.e., $U_1 = 2U_0$. A domain height of 2 km implies $U_1 = 1.33U_0$, whereas a 10 km domain height leads to $U_1 = 1.05U_0$. Unfortunately, a 10 km domain introduces numerical instabilities in the solver, most likely due to a high number of very large computational cells. As a result, a smaller domain height of 4 km is chosen, giving $U_1 = 1.14U_0$ for the two-dimensional hill, i.e., an increase in velocity of 14 %. For three-dimensional hills, however, U_1 will be significantly closer to U_0, while also introducing some degree of flow curvature in the horizontal plane, “around” the hills.

For general geophysical wind simulations, it is not necessarily an objective to minimize the large-scale effects of topography; within the atmospheric boundary layer, the topography can affect the mesoscale wind field to a large degree and should thus be present in certain simulations. However, in the present context, it is more important that the mesoscale wind vector field is homogenous throughout the domain, so that the look-up procedure from CT-Analyst is mapping the correct data one-to-one. The wind direction specified in CT-Analyst is usually based on local weather forecasting anyway, which inherently includes mesoscale (as well as synaptic scale) effects; such effects is thus not necessary (or even desired) in the micrometeorology simulated in Project 1394.[11]

6.6 Forest canopies

Only forest canopies have been considered in Project 1394. Other vegetation, such as single trees and small thickets, grasslands, grain fields or bushland can be considered negligible for urban dispersion on larger scales, given that the areas of such vegetation are small or have a minor influence relative to surrounding buildings.

Forest canopies significantly alters the turbulence and flow within the canopy (Finnigan, 2000). A forest-canopy model has been implemented in the present project, using a momentum-sink model (cf. e.g. Dwyer et al., 1997), in which a sink term,

$$F_{\mathrm{f},i} = \begin{cases} -C_d \alpha_{\mathrm{LA}} u_i \sqrt{u_j u_j}, & \text{if } z < H_\mathrm{f} \text{ and } (x, y) \in A_\mathrm{f}, \\ 0 & \text{otherwise,} \end{cases}$$

is added to Eq. (4.1). Here, C_d is a representative drag coefficient, α_{LA} is the leaf-area density, and H_f is the canopy height. In general, these three model parameters can vary in space, but in the present implementation, constant values are assumed within forested areas. A_f represents the

---

[11] The required microscale effects of topography (and buildings), such as flow recirculation and vortex shedding, is accounted for regardless of domain height.

forested areas, i.e., all computational points enclosed by the forest-canopy boundary.[12] In practice, A_f is defined via an input file to the simulation, generated from GIS forestry data.

Unfortunately, the forest canopy data for Oslo is deemed inadequate for trustworthy simulation results; there simply is not enough empirical data about the forested areas to make the model results adequately reliable. As an example, only rough distinctions between coniferous and deciduous forests are made in the GIS data. Information about tree height, drag coefficients, and leaf area density is completely absent. This would imply numerous highly uncertain assumptions about the forest canopies which were to be modeled.

That said, preliminary test simulations indicate that the presence of typical forest canopies in and near urban areas have only little to medium effect on the dispersion of hazmats when compared to the effect of nearby buildings (see Appendix B for examples). Moreover, during winter, the effect of forest canopies will be significantly less than in the summer.

In conclusion, while the ability to model forests has been implemented during Project 1394, the empirical data for forestry in Oslo is lacking. Additionally, test data indicates that the effects of forest canopies might be relatively insignificant. As a result, vegetation is not included in any of the simulations reported in the following.

6.7 Water surfaces

Dynamic influences from water surfaces, such as rivers, lakes, or oceans, are beyond the scope of this project. Such effects may include kinematic boundaries due to streaming water or waves, roughness from waves, or thermal effects from water temperatures different from the air temperature.

In principle, all these effects are possible to incorporate, although the latter is probably the most significant. Nevertheless, for practical reasons, further investigations into this matter are excluded from the present project.

6.8 Final case parameters

Based on investigations of parameter sensitivity, literature recommendations, practical considerations and experience, as discussed at length in preceding sections, the final choice of simulation parameters was made, as listed in Table 6.7. The parameters are identical for all the 18 simulations of different wind directions, except the total number of computational nodes, for which the smallest and largest meshes are given, and the wind direction, for which all the 18 directions are indicated.

Figure 6.12 illustrates the mesh resolution visually for an area in downtown Oslo with the mesh criteria given in Table 6.7. The range of cell sizes on the ground and buildings is apparent in the figure.

The inflow for each wind-direction simulation corresponds to a mean flow field of magnitude U_in in the direction normal to the inlet, as given in Table 6.7. Here, $U_0 = 7$ m/s, $\alpha = 0.25$, and the scaled vertical parameter is given by $\zeta(x, y) = \min\{(z - z_g)/(z_\delta - z_g), 1\}$, where z_g is the local ground elevation at location (x, y) and $z_\delta = 500$ m is the atmospheric boundary-layer thickness (above sea level). Turbulent fluctuations are superposed on the instantenous inflow field as described in Section 6.4, but with ζ as the scaled vertical parameter (instead of Z). Even though the displacement thickness is implicitly set to zero for the inflow described in the above, a nonzero displacement thickness is trivial to include if desired.

---

[12] A_f may consist of several disconnected regions.

Table 6.7 Simulation parameters for the final Oslo simulation setup. The top portion of the table (rows 1–5) refers to the area of interest only.

Physical domain dimensions (L × W × H) [m^3]	14,500 × 11,000 × 4,000
Number of buildings	102,154
Building area-density	0.178
Average bld. area [m^2]	264.3
Average bld. height above ground [m]	6.1
Total number of computational nodes	From 42,270,160 to 47,680,287
Cell type	Tetrahedrons
Nominal cell-edge length (min, max) [m]	4, 64
Geometric cell-growth rate in volume	1.15
Inflow characteristics	Turbulent inflow with power-law mean flow; $U_{\text{in}}(z) = U_0\zeta^\alpha$
Inflow direction [°]	$\{0, 20, 40, 60, \ldots, 320, 340\}$
Computational time step, Δt [s]	0.9
Run-up period [minutes]	30
Averaging period [minutes]	120

The outlet is implemented as a standard outflow boundary, the top surface has an imposed slip condition, and the ground surface and building walls are modeled as weakly formulated no-slip boundaries.[13]

Note that the mesh resolution given in Table 6.7 is slightly coarser than the recommendations from the previous report (Fossum and Helgeland, 2017), whereas the domain height has been extended.

---

[13] Note that at the time of writing, the CFD data in the most recent version of CT-Analyst Oslo is based the strong no-slip formulation, as well as only 60 minutes of temporal averaging. This will be updated in any future versions of the software.

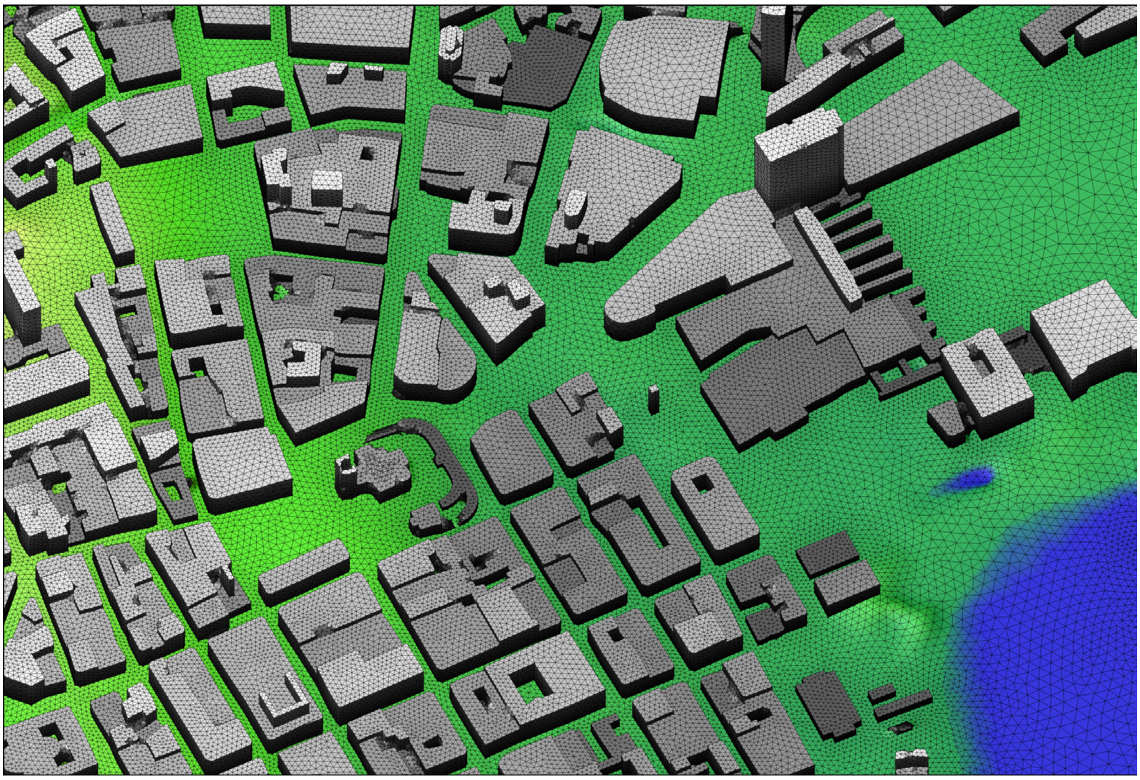

Figure 6.12 The computational mesh shown for a small part of downtown Oslo. The cell edges are shown in black, and the surfaces are colored by local elevation (from blue to light green on the ground and from black to white on the buildings).

PART III

Results

7 About the results

As discussed in Part I, FFI Project 1394 is motivated by developing a capability to run high-fidelity CFD simulations for large and realistic geographical areas, such as Oslo, as well as the production of an Oslo pilot version of the CT-Analyst software.

In light of this, the results shown and discussed in this chapter merely exemplifies the kinds of data that are available from such CFD simulations. A myriad of other ways of extracting and processing data is also available if desired. The following examples demonstrate that high-fidelity CFD data has indeed been generated for the Oslo region during the project.

In the following, the terms “global wind” and “meteorological wind” are used interchangeably and refer to the inflow direction of the simulation under disussion.

Only results pertaining to the flow field are considered. Examples of scalar transport are dicussed in a future report.

8 Flow field

8.1 Ground-level wind

To appreciate the scope of wind flow in a 150 km^2 urban region, different magnifications of the flow domain can be examined.

Figure 8.1 shows contours of the mean velocity magnitude in the entire region of interest for Oslo. The contours are shown in a surface 4 meters above ground level (i.e., following the topography) and is regarded as ground-level wind in the present context.

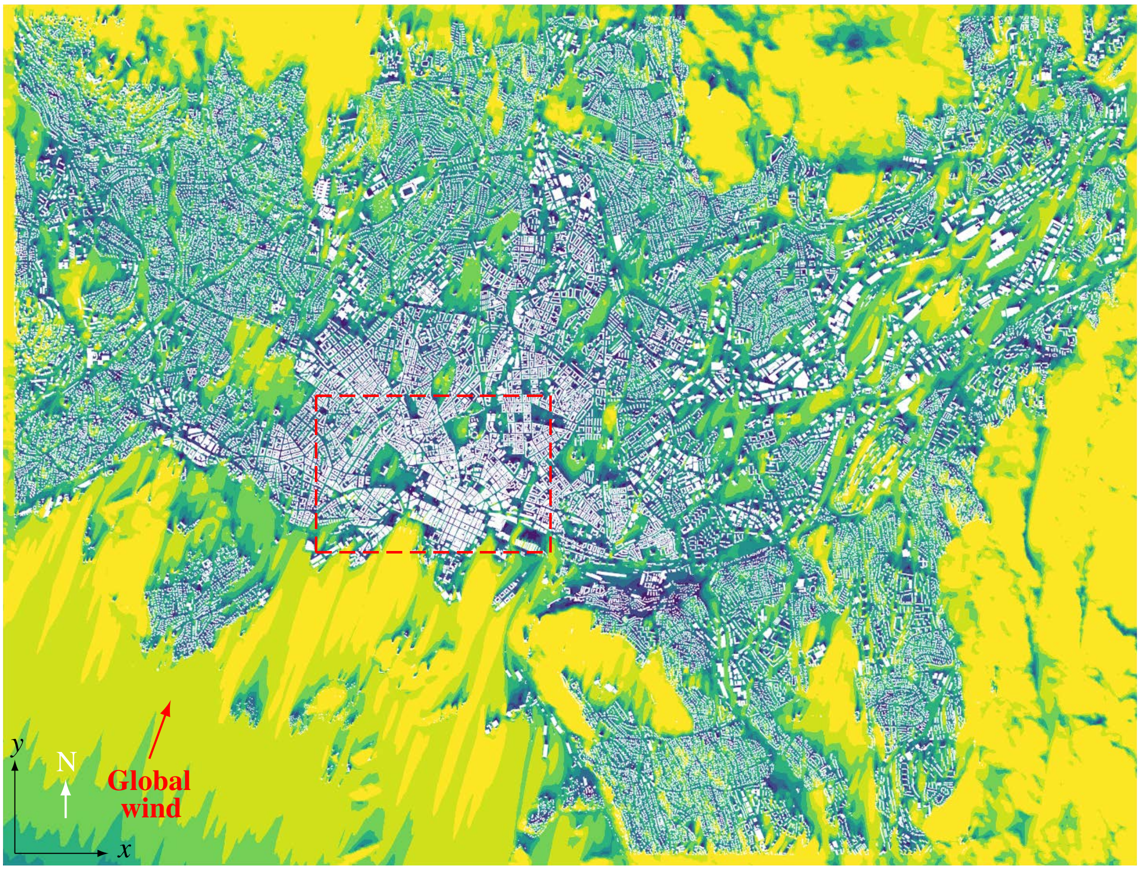

Figure 8.1 Mean velocity magnitude contours 4 m above ground level in the area of interest with 200° global wind (shown as red arrow). Contour levels (colored from dark blue through green to yellow) range from < 0.125 to > 3.5 m/s with a 0.5 m/s increase at every successive level. Buildings are shown in white.

As expected, the velocity magnitude, i.e., the wind speed, show little variation when there is no topography or buildings, such as over the fjord in the southwestern corner of the map. Within the built regions, the flow field is highly chaotic, due to the complexity of the geometry. It is also evident that the urban area slows the wind down considerably.

There also exist regions with mainly topographic influences, such as the southeastern and north-northeastern areas. In such places, it is possible to infer approximate variations in the landscape by considering the wind field; hills induce an increased wind speed, whereas the wind speeds in valleys are lower. Adjacent to the numerous small islands in the Oslo fjord, leeward regions of “velocity shadows” align with the global wind direction. These regions typically correspond to recirculation regions downwind of the islands.

In Figure 8.2, the subregion marked by red, dashed lines in Figure 8.1 is shown in a magnified view. Here, the geometric details are more clearly visible. More detailed flow patterns are also apparent, perhaps except from the flow field in narrow streets. Here, signs of leeward recirculation regions similar to those in Figure 8.1 can be observed downwind of individual building blocks.

Figure 8.2 Enlargement of the subset marked by red, dashed lines in Figure 8.1.

Figure 8.2 shows indications of the urban flow features discussed in Section 5.2.1; in particular, there is evidence of the Venturi effect in several street channels. The view shown in this figure can be further magnified; the area within the red, dashed rectangle is enlarged in Figure 8.3.

In Figure 8.3, most flow details are evident. Broadly speaking, in areas with high urban roughness, i.e., a lot of geometric structure, the wind speed is relatively lower than in more open areas. Some narrow streets, particularly those that are closely aligned with the global wind direction, also show higher speeds, due to the Venturi effect.

The overall impression from the three different views of the same flow field is that of a chaotic field, both at large and small scales. It can be expected, however, that with increasing height above ground level, the spatial structure of the wind field gradually decreases in complexity.

8.1.0.1 Local wind directions for different global directions.

In the preceding section, only wind speed was evaluated. Wind direction is more difficult to visualize, in part because it is inherently three-componential. In Figure 8.4, the mean horizontal

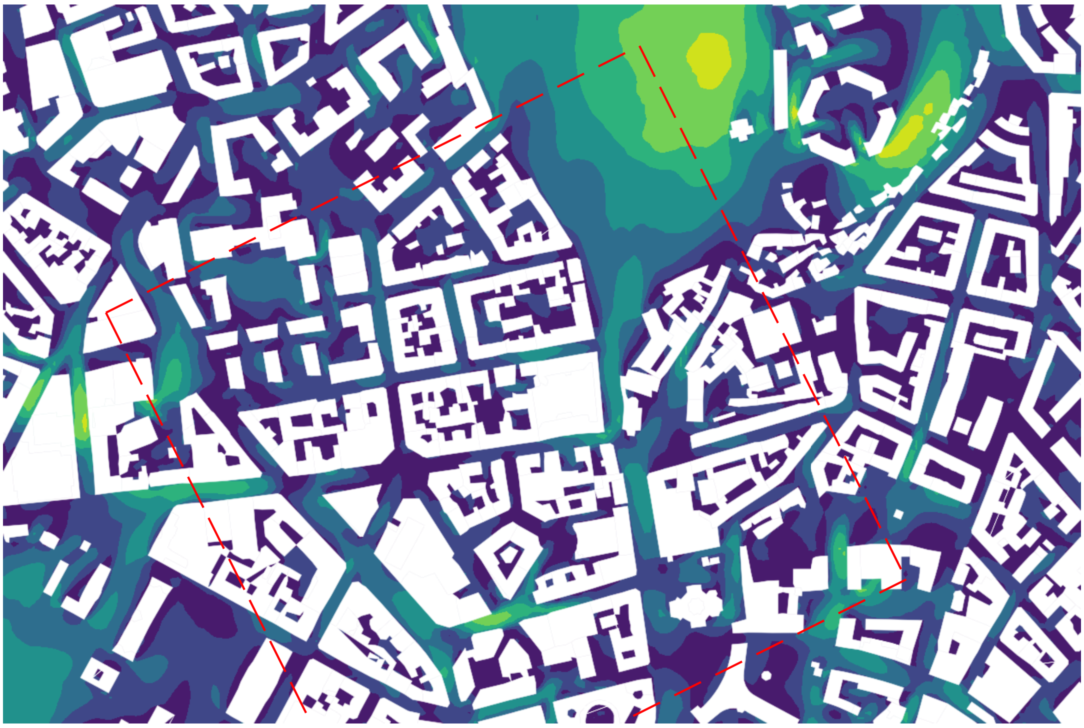

Figure 8.3 Enlargement of the subset marked by red, dashed lines in Figure 8.2.

velocity direction near the ground is shown for three different global wind directions.

As expected, the flow fields appear rather chaotic, with a wide range of local wind directions. Each flow field as a whole is a complex composite of the different urban flow features discussed earlier (cf. Section 5.2.1); in particular, regions affected by recirculation, street channeling and the Venturi effect can be identified.

Note also that when comparing the three different global wind directions, it is clear that for open areas, the local wind direction aligns rather closely with the global direction. In more confined areas, on the other hand, local wind is to a large degree controlled by local geometric features, such as street directions.

This indicates that an angular resolution of 20°, used in CT-Analyst, is sufficient, and that interpolation of the 18 CFD data sets to enable arbitrary choices of the global wind direction can be expected to be reasonably accurate.[14]

As documented in another report within Project 1394 (Fossum and Helgeland, 2019, in Norwegian), the information inherent in all the 18 CFD wind-direction sets can also be used to compute local wind roses. The local wind roses are computed by using (local) wind statistics from the CFD simulation data in conjunction with global wind roses from one or several weather-measurement stations. Examples of such roses are shown in Figure 8.6, showing different local wind roses for the positions denoted in Figure 8.5.

Local wind roses can be used to evaluate local wind statistics based on real-world global (large-scale) wind statistics by means of CFD. This may yield benefits for urban planning, wind-comfort

---

[14] This can be verified quantatively, e.g., by simulating an intermediate global-wind direction and comparing it to interpolated data. That is, however, beyond the scope of the present study.

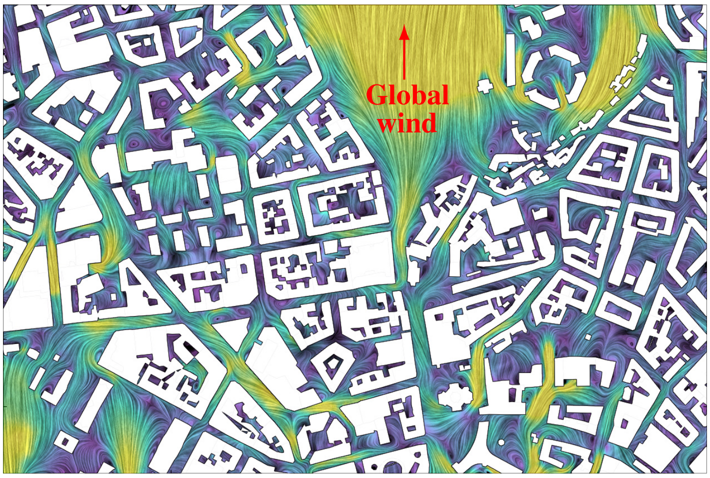

(a) 180° global wind.

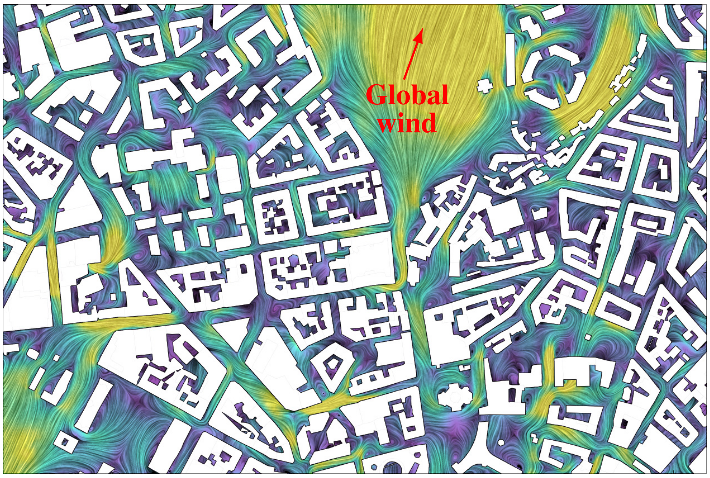

(b) 200° global wind.

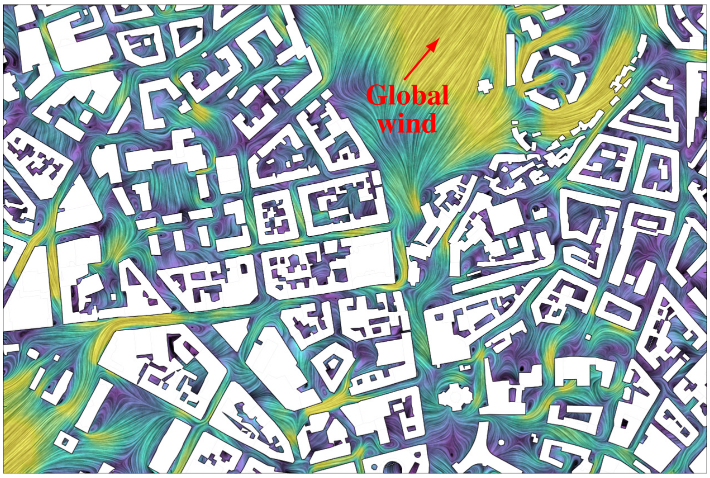

(c) 220° global wind.

Figure 8.4 Mean velocity fields 4 m above ground level for three global wind directions. Velocity magnitudes are shown with color, from dark blue (≈ 0 m/s) to yellow (> 2 m/s). Wind directions are illustrated by line-integral convolution (Cabral and Leedom, 1993). The global wind directions are shown by red arrows at the top of each subfigure.

Figure 8.5 Positions where local wind roses are computed. Position A is outside of the area shown in the figure and thus shown transparently in the lower left corner.

assessments, risk analyses, etc., that coarser meteorological wind-rose statistics or CFD simulations with only one meteorological wind direction cannot provide alone.

A final comment in this section regards the wind field at higher elevations. Figure 8.7 shows the angular deviation of horizontally averaged mean wind direction at 150 m above ground level from the inlet wind direction. Ideally, this deviation should be small, so that the inlet wind indeed forces the expected free-stream wind in the entire domain. Only then can the inlet wind and the global wind truly be considered the same.

Certain directions show a higher systematic turning of the wind than others, although all deviations are relatively small. At higher elevations (not shown) the deviations decrease.

There seems to be a gradual change in deviations as the global wind direction changes, i.e., there is a correlation in the mean angular deviation between successive global wind directions. The reason for this is not yet clear, but likely it is associated with the topography in the domain, which slightly favors some wind directions over others.

8.2 Streamlines

The flow field in an urban environment is highly three-dimensional. Although two-dimensional streamlines can be computed (illustrated in Figure 8.4), three-dimensional streamlines might better capture the complexity of the flow.

As the real flow also is highly transient, the most realistic three-dimensional streamlines would be generated by tracing fluid particles following the instantenous flow. However, those streamtraces would only capture one flow realization, which might not be representative of the “typical” flow pattern.

Hence streamlines based on the mean flow field will be considered in the following. While such streamlines do not correspond to any path actually travelled by a real fluid particle, it gives a more representative view of the average flow structures. Figure 8.8 shows a selection of such

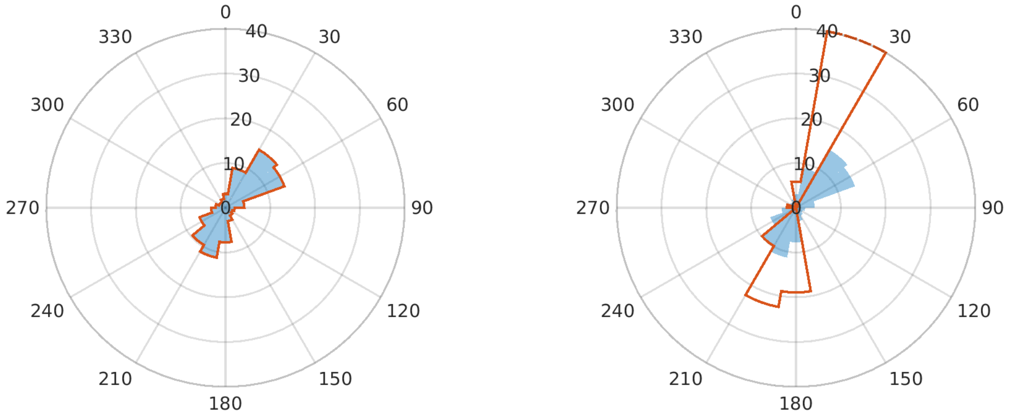

(a) The Oslo fjord.

(b) Street canyon aligned NNE, *Kongens gate*.

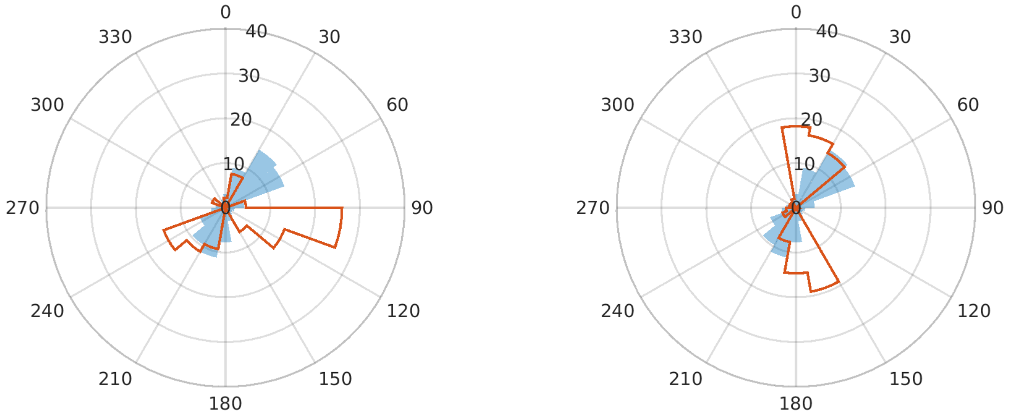

(c) Street canyon aligned WNW, *Prinsens gate*.

(d) Street crossing, *Prinsens gate/Kirkegata*.

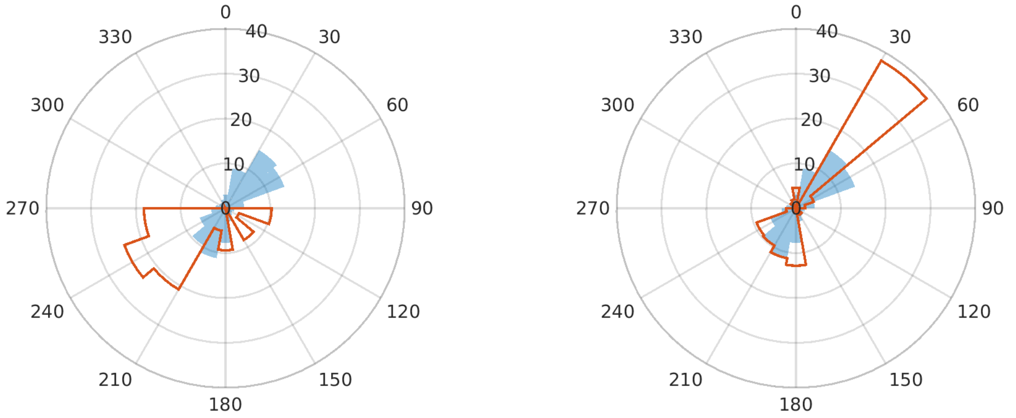

(e) Street canyon, *Smeltedigelen* in Kværnerbyen.

(f) Open space in Lodalen.

Figure 8.6 Local wind roses for selected points in Oslo, cf. Figure 8.5. Red-colored wind roses are local, whereas blue-colored roses represent the global Oslo wind rose (an average of three relevant measurement stations) and are shown as reference. Figure from Fossum and Helgeland (2019).

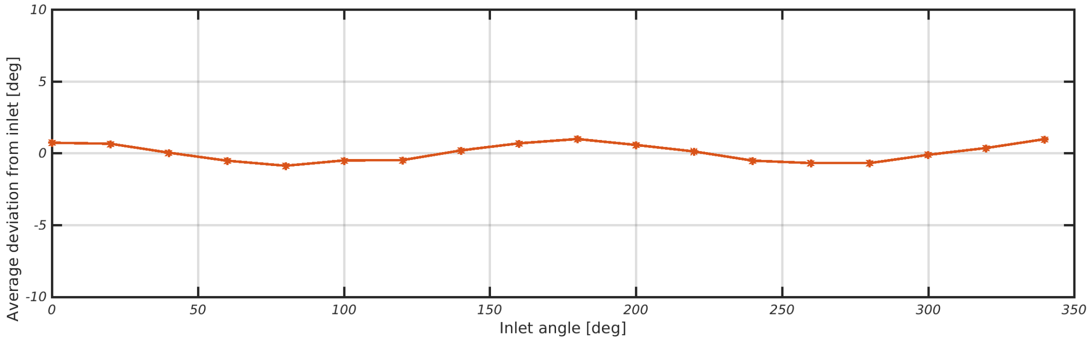

Figure 8.7 Deviation in horizontally averaged mean wind direction at 150 m above ground level from inlet wind direction.

three-dimensional streamlines in a simulation with a global wind direction of 200°. Considering the variety and apparent arbitrary twists and turns of the streamlines, it should not be hard to appreciate the difficulty of predicting details of urban flows.

From the figure, the chaotic nature of urban flow is evident. Several locations are marked by numbered circles in the figure, referring to typical urban flow phenomena listed in the following.

1. The helical street-channeled flow shown here, reminiscent of a corkscrew, is a typical urban flow feature, arising when the global wind direction is at an intermediate angle to the axis of the street canyon (Oke et al., 2017, p. 90).
2. Here, two incoming streamlines diverge, indicating a stagnation point (caused by a building) which leads to flow divergence. Both streamlines subsequently display a period of counterflow before ultimately realigning more or less with the global wind directions.
3. At this location, an example of persisting helical motion through a street of several hundred meters is observed.
4. This is an example of a recirculation region in (semi-)confined space. In the context of dispersion, such regions may “trap” contaminants for significant periods of time.
5. This streamline first makes a sharp turn around a building, due to a low-pressure region in the building’s wake, then heads in a direction perpendicular to the global wind direction for a short distance, before ascending above the buldings and realigning with the global wind.

In Figure 8.8, the streamlines are colored by elevation above ground. If colored by speed instead, the Venturi effect would also have been observed in several streets.

8.3 Turbulence

As a brief example of the turbulence distribution near the ground, Figure 8.9 shows the turbulence kinetic energy (TKE), $k = \frac{1}{2}\langle u_i u_i \rangle$. The TKE is a measure of the turbulence in the flow, and an indication of the importance of turbulent diffusion of both momentum and scalars (such as contaminants in the air). For this reason, CT-Analyst uses the TKE to determine the spreading angle of the plume (subject to a number of contraints, as well as global tuning).

From Figure 8.9 it is clear that there are few rules-of-thumb to estimate where turbulent velocity fluctuations dominate; certain confined spaces are highly turbulent, whereas others are not. Certain streets exhibit high levels of TKE, but other streets contain less turbulent flow. The levels of TKE are

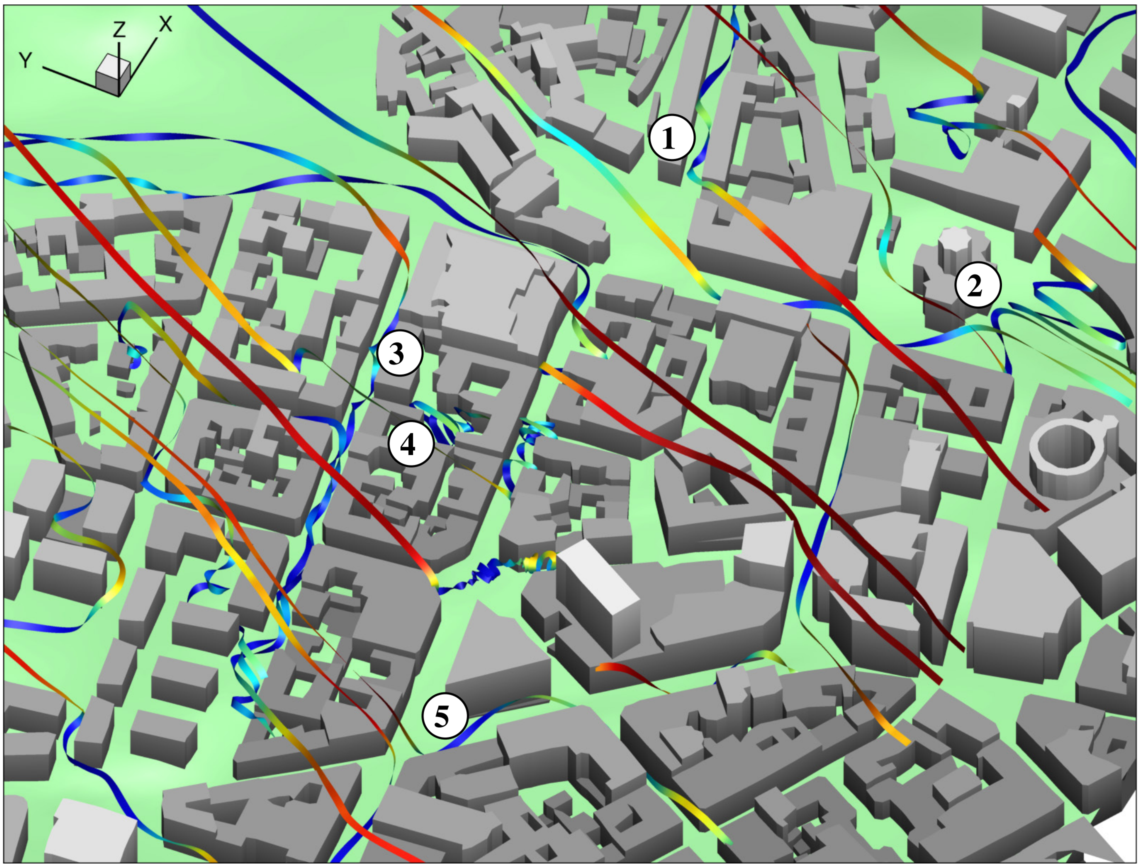

Figure 8.8 Three-dimensional streamlines in the area marked by red, dashed lines in Figure 8.3. Streamlines are colored by elevation from ground level, from dark blue (at ground) to dark red (30 m above ground).

Figure 8.9 Turbulence kinetic energy in the same region as Figure 8.3 (also marked by red, dashed lines in Figure 8.2). Data taken from the 200° global-wind simulation. Contour levels range from $\lesssim 0.03$ (dark blue) to > 1 (yellow) m^2/s^2 and the energy doubles at every successive level.

generally higher and have smaller spatial gradients at higher altitudes (not shown), as the building geometry gets sparser there, allowing higher velocities to persist.

A somewhat consistent correlation seems to exist between high TKE levels and regions of high velocity magnitude (seen in Figure 8.3), but this is by no means the case everywhere. Larger velocities generally tend to instigate more turbulence, which is why the turbulence intensity, i.e., the TKE relative to the kinetic energy of the mean flow, is sometimes considered. This is not particularly relevant in the present case.

9 Further data extraction

The preceding sections (and the previous chapter) should demonstrate that the amount of data available from the 18 entire Oslo simulations is vast. Obviously, vertical and horizontal profiles, contour plots and even three-dimensional visualizations of different data fields can be generated from the data. This will not be exemplified further here.

As mentioned in previous sections, a future report will address scalar-transport simulations in the Oslo geometry. For now, Figure 9.1 serves as an example, showing that such scalar transport processes have already been successfully simulated in the Oslo case. Data from such simulations are not strictly necessary to build CT-Analyst, but it is beneficial for setting up the optimal global parameters of the software.

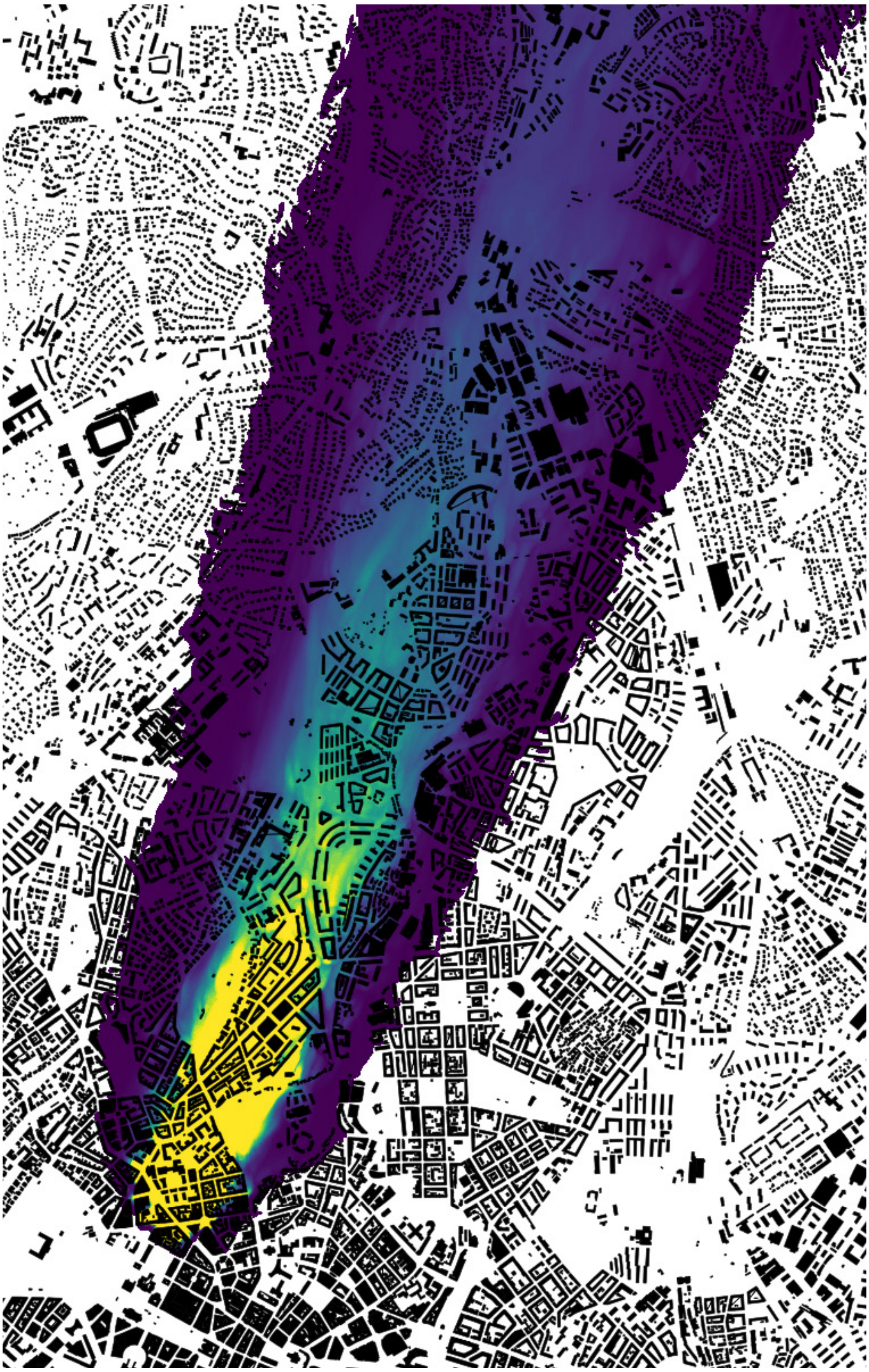

Figure 9.1 Local maximum recorded concentration for a release in downtown Oslo. Buildings are shown in black (with the Royal Palace in the southeastern corner), concentration levels range from 10^{-6} (purple) to 10^{-2} (yellow). Concentrations below the lower-cutoff are blanked (i.e., shown as white). The global wind direction is 200°.

PART IV

Concluding remarks

10 Concluding remarks

The methodology and parameters used for high-fidelity computational fluid dynamics (CFD) simulations of wind in large urban areas have been discussed. Local flow resulting from 18 different meteorological wind directions have been simulated with the selected methodology for a 150 km^2 area of Oslo. The guidelines and workflow discussed here are relevant to many cases in which CFD simulations of a geographical area is of interest.

Reported results have exemplified flow data from selected simulated global wind directions, including contour plots, three-dimensional streamlines, and local wind roses. The results have also been related to typical urban-flow features.

Through investigation of the necessary problem parameters, important findings have been reported: Although a mesh resolution of 1 m close to solid surfaces is recommended, a 2 to 4 m resolution suffices for the specific context of this work. Further, it is shown that the details of a turbulent inflow is not essential. On the other hand, the domain height and wall boundary-conditions have noticable impacts on the solution; a domain height of 4 km was sufficient for the present case, and weakly imposed wall-boundary conditions perform somewhat better than strongly imposed conditions for the finite-volume solver used here.

Applying the methodology described here, 18 different simulations of urban wind in Oslo were successfully computed and used in the generation of an operational hazmat dispersion tool, CT-Analyst® Oslo, as shown in Figure 10.1.[15]

Future work will first and foremost revolve around an investigation into scalar transport simulations. Particularly, necessary mesh resolution requirements will be determined and discussed in a separate report. Also, a study of dense-gas releases will be documented in order to provide tabular values for source characteristics in CT-Analyst. Further ahead, more in-depth studies of effects of forests, a stronger coupling to mesoscale meteorology, or investigating potential rain or traffic models may be relevant.

---

[15] The Oslo version of CT-Analyst is stil considered a pilot at this point, as final global tuning and full validation has not yet been completed.

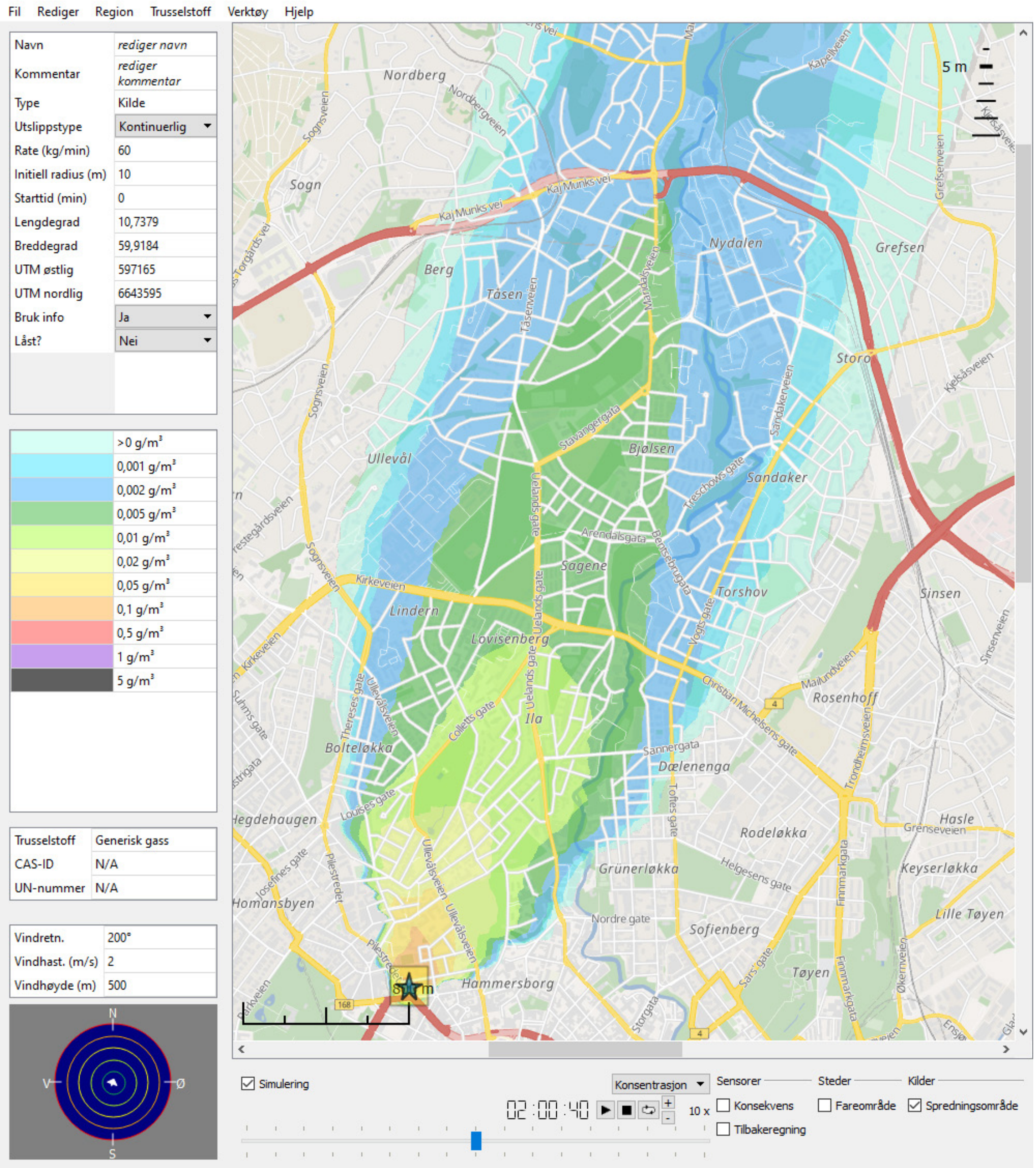

Navn	*rediger navn*
Kommentar	*rediger kommentar*
Type	Kilde
Utslippstype	Kontinuerlig
Rate (kg/min)	60
Initiell radius (m)	10
Starttid (min)	0
Lengdegrad	10,7379
Breddegrad	59,9184
UTM østlig	597165
UTM nordlig	6643595
Bruk info	Ja
Låst?	Nei

🟦	>0 g/m³
🟦	0,001 g/m³
🟦	0,002 g/m³
🟩	0,005 g/m³
🟩	0,01 g/m³
🟨	0,02 g/m³
🟨	0,05 g/m³
🟧	0,1 g/m³
🟥	0,5 g/m³
🟪	1 g/m³
⬛	5 g/m³

Trusselstoff	Generisk gass
CAS-ID	N/A
UN-nummer	N/A

Vindretn.	200°
Vindhast. (m/s)	2
Vindhøyde (m)	500

☑ Simulering

02:00:40 10 x

☐ Konsekvens ☐ Fareområde ☑ Spredningsområde

☐ Tilbakeregning

Figure 10.1 A screenshot from CT-Analyst® Oslo, based on FFI simulations with the methodology documented in this report. The source characteristics and meterological wind direction (200°) is the same as those used for the data shown in Figure 9.1.

References

American Institute of Aeronautics and Astronautics. AIAA Guide for the Verification and Validation of Computational Fluid Dynamics Simulations. 1998.

Bazilevs, Y. and Hughes, T. J. Weak imposition of Dirichlet boundary conditions in fluid mechanics. *Computers & Fluids*, 36 (1):12–26, 2007.

Beranek, W. v. and Van Koten, H. Beperken van windhinder om gebouwen, deel 1. Deventer: Stichting Bouwresearch no. 65. 1979.

Blocken, B. Computational fluid dynamics for urban physics: Importance, scales, possibilities, limitations and ten tips and tricks towards accurate and reliable simulations. *Building and Environment*, 91:219–245, 2015.

Blocken, B., Tominaga, Y., and Stathopoulos, T. CFD simulation of micro-scale pollutant dispersion in the built environment. *Building and Environment*, 64:225–230, 2013.

Boris, J., Fulton, J. E., Obenschain, K., Patnaik, G., and Young, T. CT-Analyst: Fast and accurate CBR emergency assessment. In *Proceedings of SPIE*, vol. 5416, pp. 1–13 (2004).

Boris, J., Patnaik, G., and Obenschain, K. The How and Why of Nomografs for CT-Analyst. Tech. rep., Naval Research Lab, Washington DC: Lab for Computational Physics and Fluid Dynamics, 2011.

Britter, R. and Schatzmann, M. Model Evaluation Guidance and Protocol Document COST Action 732. COST Office Brussels. 2007.

Cabral, B. and Leedom, L. C. Imaging vector fields using line integral convolution. In *Proceedings of the 20th annual conference on Computer graphics and interactive techniques*, pp. 263–270 (ACM, 1993).

Coirier, W. J., Fricker, D. M., Furmanczyk, M., and Kim, S. A computational fluid dynamics approach for urban area transport and dispersion modeling. *Environ. Fluid Dyn.*, 5:443–479, 2005.

COST Action ES1006. *COST ES1006 – Best Practice Guidelines* (2015).

Cui, P.-Y., Li, Z., and Tao, W.-Q. Numerical investigations on Re-independence for the turbulent flow and pollutant dispersion under the urban boundary layer with some experimental validations. *International Journal of Heat and Mass Transfer*, 106:422–436, 2017.

Dai, Y., Mak, C. M., Ai, Z., and Hang, J. Evaluation of computational and physical parameters influencing CFD simulations of pollutant dispersion in building arrays. *Building and Environment*, 137:90–107, 2018.

Durbin, P. A. and Petterson Reif, B. A. *Statistical Theory and Modeling for Turbulent Flows, Second Ed.* (John Wiley & Sons Ltd, West Sussex, England, 2011).

Dwyer, M. J., Patton, E. G., and Shaw, R. H. Turbulent kinetic energy budgets from a large-eddy simulation of airflow above and within a forest canopy. *Boundary-Layer Meteorology*, 84 (1):23–43, 1997.

Fernando, H. *Handbook of Environmental Fluid Dynamics, Volume Two: Systems, Pollution, Modeling, and Measurements* (CRC Press, 2012). ISBN 9781466556041.

Finnigan, J. Turbulence in plant canopies. *Annual review of fluid mechanics*, 32 (1):519–571, 2000.

Fossum, H., Dybwad, M., and Helgeland, A. Computational modeling of health effects from indoor dispersion of airborne biological and chemical agents (18/02185). Tech. rep., Forsvarets Forskningsinstitutt, 2018.

Fossum, H. and Helgeland, A. Creating computational meshes from geographical information-system data for urban environments (17/16283). Tech. rep., Forsvarets Forskningsinstitutt, 2017.

Fossum, H. and Helgeland, A. Eksempelstudie for Statens Vegvesen Vegdirektoratet: Vind- og spredningssimuleringer (19/00651). Tech. rep., Forsvarets Forskningsinstitutt, 2019.

Fossum, H., Reif, B., Tutkun, M., and Gjesdal, T. On the use of computational fluid dynamics to investigate aerosol dispersion in an industrial environment: A case study. *Boundary-Layer Meteorology*, 144:21–40, 2012.

Franke, J., Hellsten, A., Heinke Schlünchen, K., and Carissimo, B. The COST 732 Best Practice Guideline for CFD simulation of flows in the urban environment: A summary. *Int. J. Environ. and Pollut.*, 44 (1/2/3/4):419–427, 2011.

García-Sánchez, C., van Beeck, J., and Gorlé, C. Predictive large eddy simulations for urban flows: Challenges and opportunities. *Building and Environment*, 139:146–156, 2018.

García-Sánchez, C. and Gorlé, C. Uncertainty quantification for microscale CFD simulations based on input from mesoscale codes. *Journal of Wind Engineering and Industrial Aerodynamics*, 176:87–97, 2018.

Gjesdal, T., Helgeland, A., Vik, T., Petterson Reif, B. A., and Endregard, M. Simulering av utslipp og spredning fra et lagringsanlegg for svoveldioksid. Tech. rep., Tech. Rep. 2013/02880, Forsvarets Forskningsinstitutt, 2013.

Gousseau, P., Blocken, B., Stathopoulos, T., and Van Heijst, G. CFD simulation of near-field pollutant dispersion on a high-resolution grid: A case study by LES and RANS for a building group in downtown Montreal. *Atmospheric Environment*, 45 (2):428–438, 2011.

Gresho, P. M. Incompressible fluid dynamics: Some fundamental formulation issues. *Annual Review of Fluid Mechanics*, 23 (1):413–453, 1991.

Ham, F. and Iaccarino, G. Energy conservation in collocated discretization schemes on unstructured meshes. *Annual Research Briefs*, 2004:3–14, 2004.

Ham, F., Mattsson, K., and Iaccarino, G. Accurate and stable finite volume operators for unstructured flow solvers. Tech. rep., Center for Turbulence Research, 2006.

Hanna, S. and Chang, J. Acceptance criteria for urban dispersion model evaluation. *Meteorology and Atmospheric Physics*, 116 (3-4):133–146, 2012.

Hanna, S. R., Brown, M. J., Camelli, F. E., Chan, S. T., Coirier, W. J., Hansen, O. R., Huber, A. H., Kim, S., and Reynolds, R. M. Detailed simulations of atmospheric flow and dispersion in downtown Manhattan: An application of five computational fluid dynamics models. *Bulletin of the American Meteorological Society*, 87 (12):1713–1726, 2006.

Hanna, S. R., Hansen, O. R., and Dharmavaram, S. FLACS CFD air quality model performance evaluation with Kit Fox, MUST, Prairie Grass, and EMU observations. *Atmospheric Environment*, 38 (28):4675–4687, 2004.

Hertwig, D., Patnaik, G., and Leitl, B. LES validation of urban flow, part I: Flow statistics and frequency distributions. *Environmental Fluid Mechanics*, 17 (3):521–550, 2017a.

Hertwig, D., Patnaik, G., and Leitl, B. LES validation of urban flow, part II: Eddy statistics and flow structures. *Environmental Fluid Mechanics*, 17 (3):551–578, 2017b.

Keating, A., Piomelli, U., Balaras, E., and Kaltenbach, H.-J. A priori and a posteriori tests of inflow conditions for large-eddy simulation. *Physics of Fluids*, 16:4696, 2004.

Lateb, M., Meroney, R., Yataghene, M., Fellouah, H., Saleh, F., and Boufadel, M. On the use of numerical modelling for near-field pollutant dispersion in urban environments – a review. *Environmental Pollution*, 208:271–283, 2016.

Lien, F.-S. and Yee, E. Numerical modelling of the turbulent flow developing within and over a 3D building array, Part I: A high-resolution Reynolds-Averaged Navier-Stokes approach. *Boundary-Layer Meteorology*, 112:427–466, 2004.

Lien, F.-S., Yee, E., Ji, H., Keats, A., and Hsieh, K. J. Progress and challenges in the development of physically-based numerical models for prediction of flow and contaminant dispersion in the urban environment. *Int. J. of Comput. Fluid Dyn.*, 20:323–337, 2006.

Mahesh, K., Constantinescu, G., Apte, S., Iaccarino, G., Ham, F., and Moin, P. Progress toward large-eddy simulation of turbulent reacting and non-reacting flows in complex geometries. *Annual Research Briefs*, pp. 115–142, 2002.

Mahesh, K., Constantinescu, G., and Moin, P. A numerical method for large-eddy simulation in complex geometries. *Journal of Computational Physics*, 197:215–240, 2004.

Ministry of Justice and Public Security. Risiko i et trygt samfunn. Samfunnssikkerhet. Meld. St. 10 (2016-2017). 2016. URL `https://www.regjeringen.no/contentassets/00765f92310a433b8a7fc0d49187476f/no/pdfs/stm201620170010000dddpdfs.pdf`.

Ministry of Justice and Public Security, Ministry of Health and Care Services, Ministry of Defence. National Strategy for CBRNE-preparedness. 2016. URL `https://www.regjeringen.no/contentassets/3fe1d74dc4e94cf58d4dbc10a9c410da/nasjonal-strategi-cbrne.pdf`.

Oberkampf, W. L. and Trucano, T. G. Verification and validation in computational fluid dynamics. *Progress in aerospace sciences*, 38 (3):209–272, 2002.

Oke, T., Mills, G., Christen, A., and Voogt, J. *Urban Climates* (Cambridge University Press, 2017). ISBN 9780521849500. URL `https://books.google.no/books?id=7h0xDwAAQBAJ`.

Patnaik, G. and Boris, J. Fast and accurate CBR defense for homeland security: Bringing HPC to the first responder and warfighter. In *DoD High Performance Computing Modernization Program Users Group Conference, 2007*, pp. 120–126 (IEEE, 2007).

Patnaik, G., Boris, J., Lee, M.-Y., Young, T., Leitl, B., Harms, F., and Schatzmann, M. Validation of an LES urban aerodynamics model with model and application specific wind tunnel data. In *Proceeding of the 7th Asia-Pacific conference on wind engineering, Taipei*, pp. 8–12 (2009).

Pope, S. B. *Turbulent Flows* (Cambridge University Press, Cambridge, United Kingdom, 2000).

Pullen, J., Boris, J. P., Young, T., Patnaik, G., and Iselin, J. A comparison of contaminant plume statistics from a Gaussian puff and urban CFD model for two large cities. *Atmospheric Environment*, 39 (6):1049–1068, 2005.

Sagaut, P. *Large Eddy Simulation for Incompressible Flows: An Introduction*. Scientific Computation (Springer, 2006), 3rd ed. ISBN 9783540263449. URL `http://books.google.no/books?id=0DYiH6RNyoQC`.

Santiago, J. L., Martilli, A., and Martin, F. CFD simulation of airflow over a regular array of cubes. Part I: Three-dimensional simulation of the flow and validation with wind-tunnel experiments. *Boundary-Layer Meteorology*, 122:609–634, 2007.

Stull, R. *Practical Meteorology: An Algebra-Based Survey of Atmospheric Science* (Dept. of Earth, Ocean & Atmospheric Sciences, University of British Colombia, 2017).

Tamura, T., Kawai, H., Bale, R., Onishi, K., Tsubokura, M., Kondo, K., and Nozu, T. Analysis of wind turbulence in canopy layer at large urban area using HPC database. In *Proceedings of the 9th International Conference on Urban Climate (ICUC9) jointly with 12th Symposium on the Urban Environment, Toulouse, France, 20-24 July 2015* (University of Toulouse, France, 2015).

Tolias, I., Koutsourakis, N., Hertwig, D., Efthimiou, G., Venetsanos, A., and Bartzis, J. Large eddy simulation study on the structure of turbulent flow in a complex city. *Journal of Wind Engineering and Industrial Aerodynamics*, 177:101–116, 2018.

Tominaga, Y., Mochida, A., Yoshie, R., Kataoka, H., Nozu, T., Yoshikawa, M., and Shirasawa, T. AIJ guidelines for practical applications of CFD to pedestrian wind environment around buildings. *Journal of wind engineering and industrial aerodynamics*, 96 (10-11):1749–1761, 2008.

Tominaga, Y. and Stathopoulos, T. CFD simulation of near-field pollutant dispersion in the urban environment: A review of current modeling techniques. *Atmospheric Environment*, 79:716–730, 2013.

Tominaga, Y. and Stathopoulos, T. Ten questions concerning modeling of near-field pollutant dispersion in the built environment. *Building and Environment*, 105:390–402, 2016.

Versteeg, H. K. and Malalasekera, W. *An Introduction to Computational Fluid Dynamics: The Finite Volume Method* (Pearson Education, 1995).

Vik, T., Tørnes, J., and Petterson Reif, B. Simulations of the release and dispersion of chlorine and comparison with the Jack Rabbit field trials. Tech. rep., Tech. Rep. 2015/01474, Forsvarets Forskningsinstitutt, 2015.

Wingstedt, E. M., Fossum, H. E., and Reif, B. A. P. Simulation of bomb residue deposition following the Oslo bombing July 22, 2011. Tech. rep., Tech. Rep. 2012/01836, Forsvarets Forskningsinstitutt, 2012.

Wingstedt, E. M. M., Osnes, A. N., Åkervik, E., Eriksson, D., and Reif, B. P. Large-eddy simulation of dense gas dispersion over a simplified urban area. *Atmospheric Environment*, 152:605–616, 2017.

Wu, X. Inflow turbulence generation methods. *Annual Review of Fluid Mechanics*, 49:23–49, 2017.

Wyngaard, J. *Turbulence in the Atmosphere* (Cambridge Univ Pr, 2010).

Xie, Z.-T. and Castro, I. P. Large-eddy simulation for flow and dispersion in urban streets. *Atmospheric Environment*, 43 (13):2174–2185, 2009.

A Relating the MNMB to systematic relative bias

The MNMB, cf. Section 6.2.1, can be written

$$\text{MNMB} = \frac{2}{N} \sum_i b,$$

in which

$$b = \frac{C_{t,i} - C_{r,i}}{C_{t,i} + C_{r,i}}.$$

Now, if the test data is consistently biased, i.e., $C_{t,i} = (1+\alpha)C_{r,i}$ for all i, where $\alpha \in [-1, \infty)$ is the relative over-/underprediction, we have

$$\begin{aligned} b &= \frac{(1+\alpha)C_{r,i} - C_{r,i}}{(1+\alpha)C_{r,i} + C_{r,i}} \\ &= \frac{2\alpha}{2+\alpha}. \end{aligned}$$

Rearranging yields

$$\alpha = \frac{2b}{2-b}, \tag{A.1}$$

from which equivalent consistent biases, α, can be inferred from MNMB values, b. Although the assumption of consistent bias seldom holds, Equation (A.1) nevertheless indicates the consistent-bias equivalent of the MNMB metric in general.

Table A.1 lists selected MNMB values and their consistent-bias equivalents. Note that whereas the MNMB is bounded between -2 and 2, the consistent bias range from -1 (100 % underpredicted, i.e., the test data is 0, so 100 % down from the reference data) to infinity (since the test data can be arbitrarily large compared to the reference data). This $[0, \infty) \rightarrow [-2, 2)$ mapping is just one of the benefits of the MNMB metric.

Table A.1 Selected MNMB values, b, and their consistent-bias equivalents, α.

b	α
−2	−1
−1	−0.666
−0.5	−0.400
−0.25	−0.222
−0.1	−0.095
−0.05	−0.048
0	0
0.05	0.051
0.1	0.105
0.25	0.286
0.5	0.666
1	2.000
1.9	38
1.99	398

B Tentative test simulations with forested areas

The following data is only tentative, based on simulations performed mainly to verify the forest-model implementation. There have been no validation of the forest parameters or results against external data sources, and the empirical forestry parameters tested here constitute educated guesses only.

That said, the results indicate (i) that the forest model is correctly implemented and works as expected, and (ii) that the effect of small, sparsely forested areas within larger urban areas have minor effects on the flow field and scalar transport outside of the forested regions.

Figure B.1 shows a subdomain of Oslo, 700 x 1300 m^2, in which meteorological wind from the south has been simulated. In Figure B.1a, the forest model is inactive, whereas in the three other subfigures, the forest model is activated with different parameters, as given in the figure captions.

As seen, the mean flow field within the forested areas are affected by the presence of forestry. However, outside of the forests, even relatively close, the mean flow field is not significantly affected by the forest. Furthermore, varying the specific forest parameters cause relatively small variations in the simulated flow field within forested areas near the ground. For this reason, for the remainder of this section, only the forest model with parameters given in Figure B.1b will be compared to the case with no forest model (shown in Figure B.1a).

Figure B.2 shows the velocity contours as well as selected in-plane streamlines north of the largest forested areas in the subdomain. Again, it is seen that only small differences between the mean flow fields are visible outside the forested areas.

Contours of turbulence kinetic energy, as well as vertical profiles, corroborate the findings indicated in Figure B.1 and B.2, although not shown here.

The effect of forestry on scalar transport has also been briefly investigated. Figure B.3 shows mean concentration contours for the subdomain; the most significant effect seems to be a narrowing of the concentration plume, with resulting higher centerline concentrations downstream. This effect is, however, not great.

Similar conclusions can be drawn from Figure B.4, showing the concentration contours in the northern outflow plane downstream of the forested areas. It can be seen that the general extent and shape of the plume from the simulation with no forest model are rather similar to those of the plume from the forest-model simulation.

In conclusion, the tentative results presented here suggest that the effect of forestry is negligible under the circumstances of relatively small and sparse forested areas compared to the surrounding urban landscape. However, more systematic studies on larger data sets are required in order to increase the confidence in these findings.

Finally, it should be noted that effects of forestry on the scalar transport directly, e.g., through a sink term due to leaf deposition, are not modeled. The lack of such a model is on the conservative side in terms of downstream concentration values.

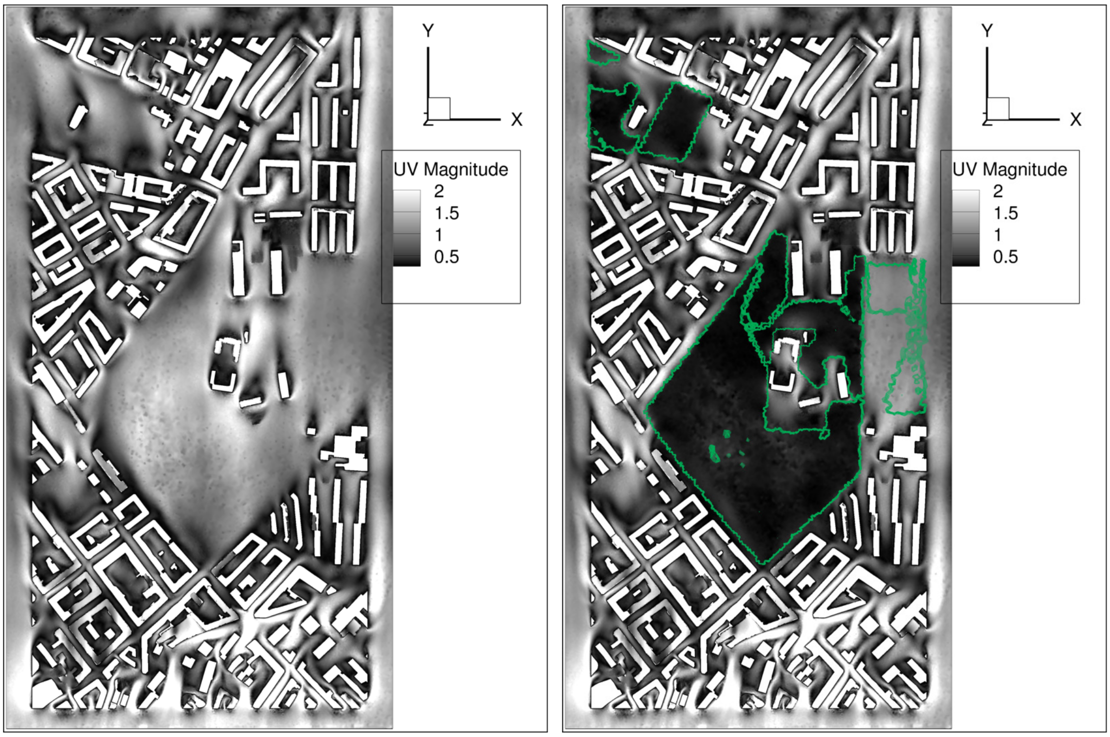

(a) No forest model.

(b) Forest model active; $C_d = 0.25$, $\alpha_{\mathrm{LA}} = 5$, and $H_{\mathrm{f}} = 10$ m.

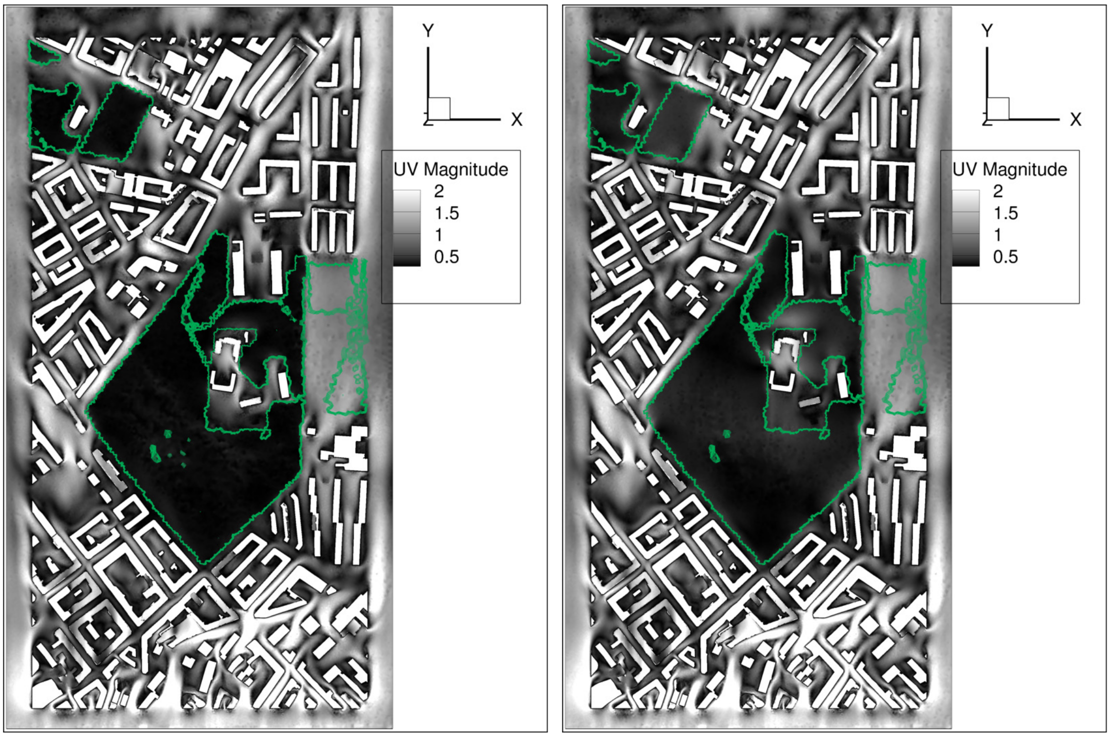

(c) Forest model active; $C_d = 0.5$, $\alpha_{\mathrm{LA}} = 10$, and $H_{\mathrm{f}} = 10$ m.

(d) Forest model active; $C_d = 0.25$, $\alpha_{\mathrm{LA}} = 5$, and $H_{\mathrm{f}} = 20$ m.

Figure B.1 Mean wind speed contours in a plane 4 m above ground for different forest-model simulations. The forested areas are enclosed by green lines. The given model parameters refer to Section 6.6.

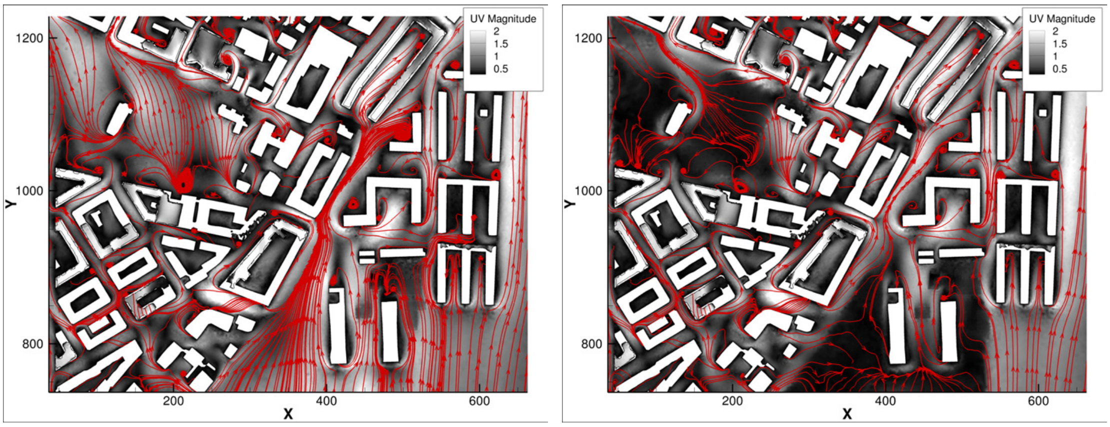

(a) No forest model.

(b) Forest model active.

Figure B.2 Mean wind speed contours in a plane 4 m above ground for different forest model simulations. Refer to Figure B.1 to see the defined forested areas.

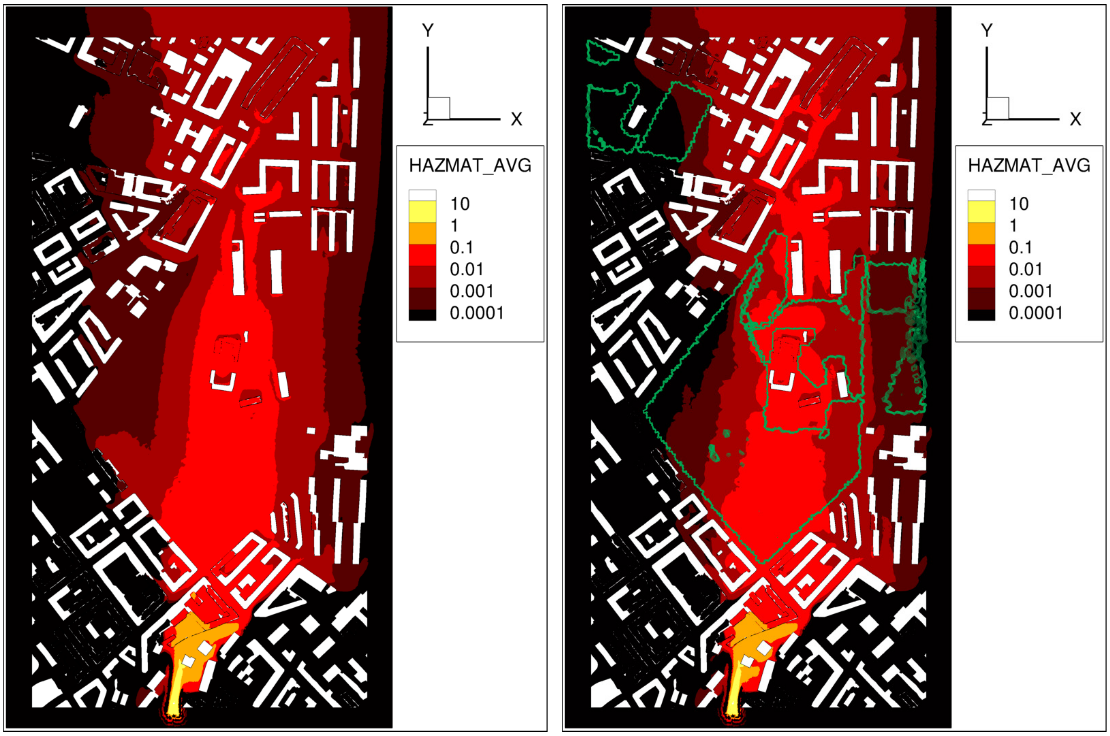

(a) No forest model.

(b) Forest model active.

Figure B.3 Mean concentration contours in a plane 4 m above ground with and without forest modeling. The forested areas are enclosed by green lines.

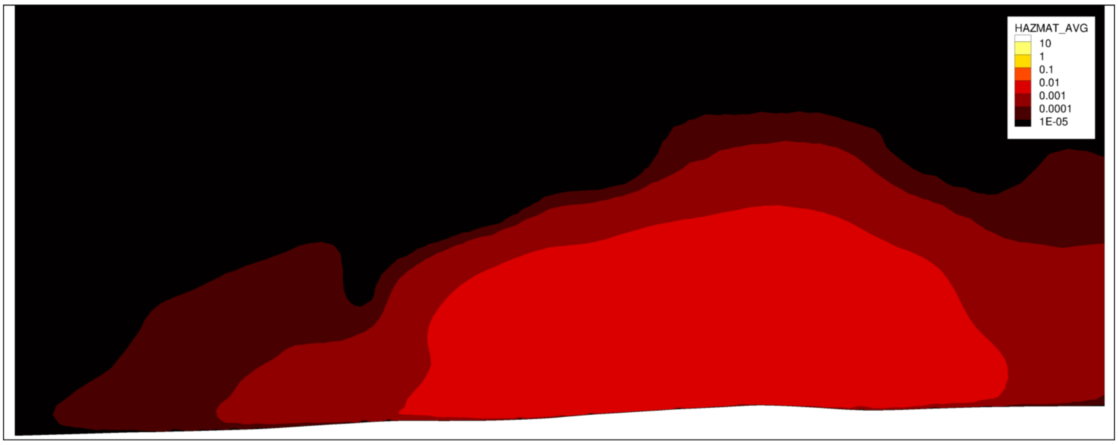

(a) No forest model.

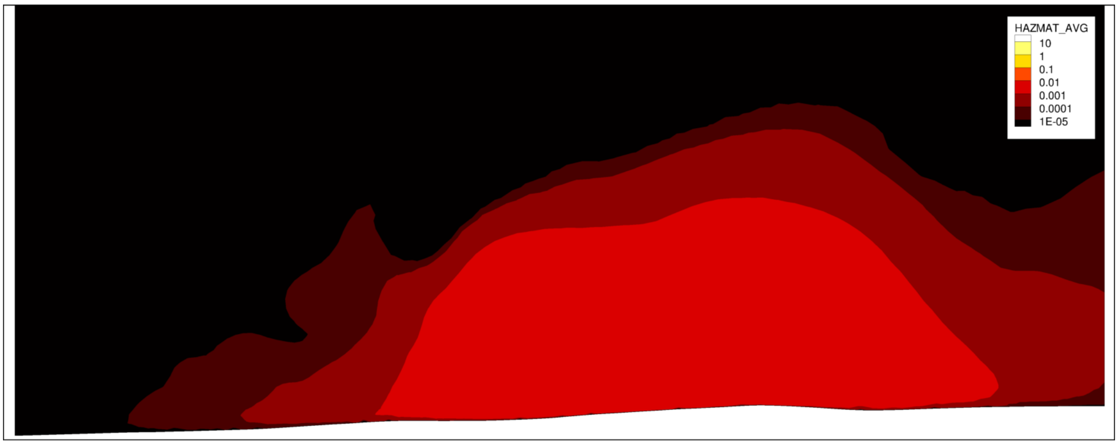

(b) Forest model active.

Figure B.4 Mean concentration contours in the outflow xz-plane with and without forest modeling. The plane is viewed from the south.

About FFI

The Norwegian Defence Research Establishment (FFI) was founded 11th of April 1946. It is organised as an administrative agency subordinate to the Ministry of Defence.

FFI's MISSION

FFI is the prime institution responsible for defence related research in Norway. Its principal mission is to carry out research and development to meet the requirements of the Armed Forces. FFI has the role of chief adviser to the political and military leadership. In particular, the institute shall focus on aspects of the development in science and technology that can influence our security policy or defence planning.

FFI's VISION

FFI turns knowledge and ideas into an efficient defence.

FFI's CHARACTERISTICS

Creative, daring, broad-minded and responsible.

Om FFI

Forsvarets forskningsinstitutt ble etablert 11. april 1946. Instituttet er organisert som et forvaltningsorgan med særskilte fullmakter underlagt Forsvarsdepartementet.

FFIs FORMÅL

Forsvarets forskningsinstitutt er Forsvarets sentrale forskningsinstitusjon og har som formål å drive forskning og utvikling for Forsvarets behov. Videre er FFI rådgiver overfor Forsvarets strategiske ledelse. Spesielt skal instituttet følge opp trekk ved vitenskapelig og militærteknisk utvikling som kan påvirke forutsetningene for sikkerhetspolitikken eller forsvarsplanleggingen.

FFIs VISJON

FFI gjør kunnskap og ideer til et effektivt forsvar.

FFIs VERDIER

Skapende, drivende, vidsynt og ansvarlig.

FFI's organisation

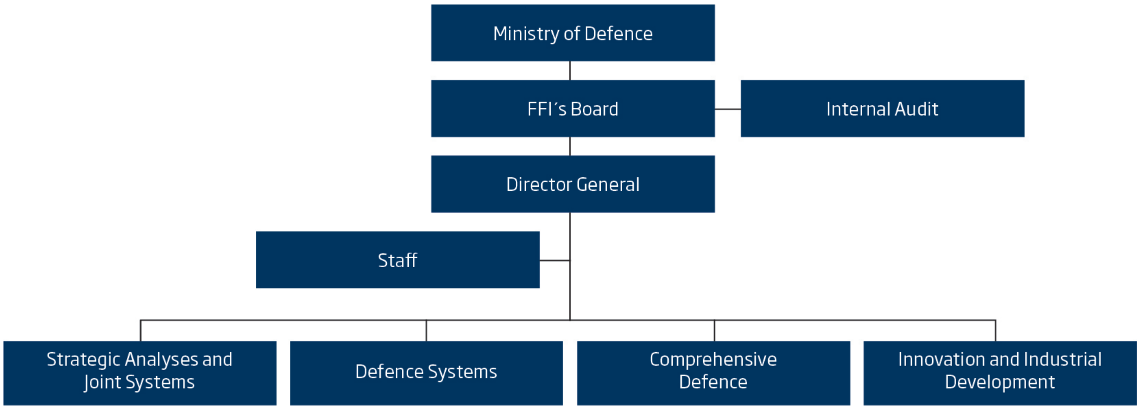

Forsvarets forskningsinstitutt
Postboks 25
2027 Kjeller

Besøksadresse:
Instituttveien 20
2007 Kjeller

Telefon: 63 80 70 00
Telefaks: 63 80 71 15
Epost: ffi@ffi.no

Norwegian Defence Research Establishment (FFI)
P.O. Box 25
NO-2027 Kjeller

Office address:
Instituttveien 20
N-2007 Kjeller

Telephone: +47 63 80 70 00
Telefax: +47 63 80 71 15
Email: ffi@ffi.no

FFI Forsvarets forskningsinstitutt
Norwegian Defence Research Establishment